


**Barkhausen noise in disordered striplike ferromagnets: Experiment versus simulations**Djordje Spasojević  and Miloš Marinković*Faculty of Physics, University of Belgrade, P. O. Box 44, 11001 Belgrade, Republic of Serbia*Dragutin Jovković *Faculty of Mining and Geology, University of Belgrade, P. O. Box 162, 11000 Belgrade, Republic of Serbia*Sanja Janičević *Faculty of Science, University of Kragujevac, P. O. Box 60, 34000 Kragujevac, Republic of Serbia*Lasse Laurson *Computational Physics Laboratory, Tampere University, P. O. Box 692, FI-33014 Tampere, Finland*Antonije Djordjević *School of Electrical Engineering, University of Belgrade, 11000 Belgrade, Republic of Serbia  
and Serbian Academy of Sciences and Arts, 11000 Belgrade, Republic of Serbia*

(Received 19 September 2023; accepted 29 January 2024; published 13 February 2024)

In this work, we present a systematic comparison of the results obtained from the low-frequency Barkhausen noise recordings in nanocrystalline samples with those from the numerical simulations of the random-field Ising model systems. We performed measurements at room temperature on a field-driven metallic glass stripe made of VITROPERM 800 R, a nanocrystalline iron-based material with an excellent combination of soft and magnetic properties, making it a cutting-edge material for a wide range of applications. Given that the Barkhausen noise emissions emerging along a hysteresis curve are stochastic and depend in general on a variety of factors (such as distribution of disorder due to impurities or defects, varied size of crystal grains, type of domain structure, driving rate of the external magnetic field, sample shape and temperature, etc.), adequate theoretical modeling is essential for their interpretation and prediction. Here the Random field Ising model, specifically its athermal nonequilibrium version with the finite driving rate, stands out as an appropriate choice due to the material's nanocrystalline structure and high Curie temperature. We performed a systematic analysis of the signal properties and magnetization avalanches comparing the outcomes of the numerical model and experiments carried out in a two-decade-wide range of the external magnetic field driving rates. Our results reveal that with a suitable choice of parameters, a considerable match with the experimental results is achieved, indicating that this model can accurately describe the Barkhausen noise features in nanocrystalline samples.

DOI: [10.1103/PhysRevE.109.024110](https://doi.org/10.1103/PhysRevE.109.024110)**I. INTRODUCTION**

A multitude of systems respond to slowly changing external conditions by exhibiting a bursty, “crackling noise” type of response, consisting of a sequence of bursts of activity, or avalanches, characterized by scale-free power-law distributions [1]. A prime example of both fundamental and applied interest is given by Barkhausen noise (BN) [2]. It consists of irregular electromotive force (EMF) pulses induced by the jumps in magnetization caused by the jerky motion of magnetic domain walls in response to the slow changes of the external magnetic field.

The BN studies performed so far [3–20] have shown that the (individual) jumps, and therefore the BN pulses, are stochastic and that their distributions follow power laws described by power-law indices which satisfy certain scaling relations. Experimental studies of Barkhausen noise have been conducted both in bulk [8] and nonequilateral geometry samples, in particular thin films [9–11]. Two distinctive

universality classes have been identified in polycrystalline and amorphous bulk materials, while in thin samples the question of universality remains to be resolved. The use of magneto-optical techniques [13] demonstrated the clear difference between the magnetic behavior of thin films and bulk materials, while more scrutinized investigations [16,17,19] confirmed the existence of various types of two-dimensional (2D) dynamics in thin films with different thicknesses. BN is by no means unique in exhibiting crackling noise with power-law statistics. Numerous other systems exhibit a similar pattern of behavior sharing the profound analogies despite fundamental differences in spatiotemporal scales, system geometry, structure, underlying interactions, and type of driving. Examples of such systems cover a broad range, including compressed nanocrystals [21], imbibition fronts in porous materials [22], plastic deformation due to collective dynamics of dislocations [23–26], heartbeat [27] and brain dynamics [28–30], earthquakes [31–33], and financial stock markets [34,35].

Theoretical or numerical models of BN proposed in the literature include discrete spin models such as the random-field Ising model (RFIM) [36–39], micromagnetic simulations [40,41], and various domain-wall models describing domain walls as driven elastic interfaces in random media [42]. The underlying field-driven system’s processes exhibit stochasticity along the hysteresis loop and are influenced by a plethora of interrelated factors such as disorder originated from impurities and defects, distribution of crystal grains, type of domain structure, driving rate of the external magnetic field, sample shape, temperature, applied stress, and so on. It is difficult to determine how relevant each of them is to the behavior of the system; therefore, choosing the most appropriate theoretical modeling is very important for understanding their significance and how they relate to one another.

In this paper, we use the field-driven athermal nonequilibrium RFIM as a model that can be considered suitable for the description of the BN emitted from the samples made of nanocrystalline metallic glass materials that is missing in the literature to our knowledge. To this end, we present a systematic comparison between the simulation results and the BN recordings performed in a two-decade-wide range of low driving rates on a sample of this material type, namely VITROPERM 800 R nanocrystalline metallic glass. We find that by tuning the disorder and driving rate parameters of the model appropriately, the model is able to reproduce most of the experimental BN features. Unlike in the equilibrium model version [43–46], in which the system evolves jumping between the equilibrium states determined by the current value of the external magnetic field, in the nonequilibrium model version, the system evolves through the nonequilibrium states following some local dynamic rule. The nonequilibrium version enables simulations of the time response of the system (mimicking BN) under all driving conditions and better corresponds to the BN experiments performed on metallic glasses which are by themselves not in equilibrium. Also, this model version is greatly computationally more efficient, so it enables simulations of much larger systems reducing the finite-size effects.

This paper is organized as follows: After the introduction in Sec. I, the details on the experimental analysis are presented in Sec. II, including Secs. II A and II B devoted to the description of the experimental setup and BN recordings. Section III showcases obtained results and contains Secs. III A and III B dedicated to the analysis of experimental BN response signals and hysteresis loops, a detailed explanation of the decomposition of BN signal into BN pulses, and experimental BN distributions, followed by Sec. III C devoted to the comparison of results of experimental BN measurements and numerical simulations of RFIM. The paper ends with discussion and conclusion presented in Sec. IV followed by Appendixes A and B.

## II. EXPERIMENTAL ANALYSIS

### A. Experimental setup

We performed the Barkhausen noise recordings using the setup depicted in Fig. 1. The Barkhausen noise signal was collected by a pickup coil (1100 turns of AWG 34 copper

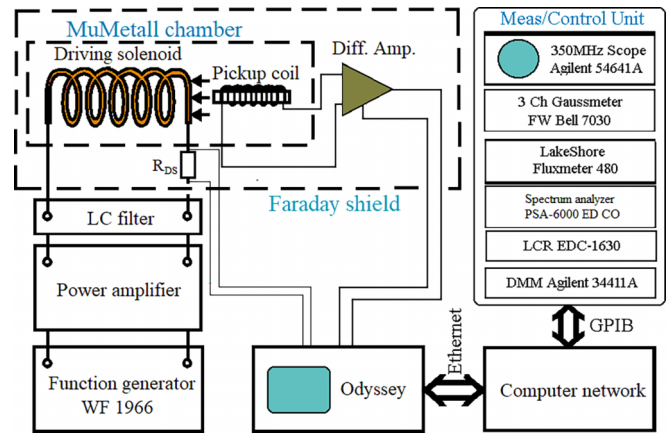


FIG. 1. Schematic presentation of the experimental setup used in our Barkhausen noise measurements.

wire 0.160 mm in diameter and  $23.3 \Omega$  resistance) tightly wound around the entire sample, see more in Appendix A. The sample and the pickup coil were placed in the middle of a 30-cm-long driving solenoid with a circular cross section 5 cm in (inner) diameter, 840 turns in three rows of AWG 26 copper wire 0.405 mm in diameter, and  $5.7 \Omega$  resistance. This driving coil provided the external magnetic field that is homogeneous along 80% of its axis with 1% tolerance due to the presence of two compensating coils (each with 50 turns of wire) placed at the driving coil ends.

The electric current, causing the external magnetic field by its flow through the driving coil, is produced at the output of a dedicated battery-operated transconductance amplifier from the input voltage signal generated by a function generator (two-channel Multifunction synthesizer WF 1966B, NF corporation, Japan, 0.01  $\mu$ Hz to 50 MHz frequency range with  $\pm 5$  ppm accuracy, 14-bit waveform resolution, and  $\pm 10$  V maximum output). The (digital high-frequency) generator voltage noise is suppressed at the amplifier input by a low-pass active filter (four stages: Sallen-Key 20 Hz cutoff frequency, 12 dB/octave each, 48 dB/octave overall), so that the standard deviation of the generated current noise was less than 20  $\mu$ A providing driving virtually without digital and environmental noise.

The response signal (i.e., the electromotive force generated in the pickup coil) is routed from the pickup coil to a laboratory-made battery-operated two-stage voltage amplifier. In its first stage a CA-261F2 Low Noise Bipolar Amplifier (NF Corporation, Japan) is used with dc to 200 kHz frequency response, gain  $40 \text{ dB} \pm 0.2 \text{ dB}$ , and equivalent input noise voltage of  $0.8 \text{ nV}/\sqrt{\text{Hz}}$ . In the second amplifier stage a National Semiconductor LME 49720NA dual high-performance, high-fidelity audio operational amplifier is used with maximum gain of 26.85 dB and equivalent input noise of  $2.7 \text{ nV}/\sqrt{\text{Hz}}$ . The measurements were performed with the overall amplifier gain set at 2100, turned on a first-order RC filter in the feedback section of the amplifier with the cutoff frequency set to 160 kHz, and the overall equivalent input noise voltage less than  $1 \text{ nV}/\sqrt{\text{Hz}}$ .

The amplified BN signal is led by a BNC cable to an OD200 acquisition card (four differential channels,

10 MHz-500 kHz maximum-continuous sampling rate on all channels, and 14-bit-16-bit resolution) of the Odyssey XE (Nicolet, USA) data acquisition system. Besides the BN signal, we also monitored on another OD200 channel the voltage at a  $R_{DS} = 1.00 \Omega$  (metal film) resistor connected in series with the driving solenoid giving us, via the conversion factor of  $2960 \text{ Am}^{-1}/\text{V}$ , the time profile of the magnetic field  $H$  inside the driving solenoid.

The sample, pickup coil, and driving solenoid were enclosed in a cylindrical MuMetall chamber (Vacuumschmelze, Germany) with four walls (each 3 mm thick) providing 50-cm-high and 35-cm-diameter shielded volume, placed together with both amplifiers inside a sealed  $1 \times 1 \times 1 \text{ m}$  sound isolated Faraday shield made of 1-cm-thick solid aluminium. Due to such shielding and battery-operated amplifiers, the recorded Barkhausen noise was virtually free from the external electromagnetic noise and pollution penetrating from the electric network, as well as from the external static and low-frequency environment electric and magnetic field.

Let us also mention that in the calibration of the measurement system and for various types of control measurements we used a 350 MHz oscilloscope (Agilent 54641A), three-channel gaussmeter (FW Bell 7030), LakeShore fluxmeter 480, 6.2-GHz spectrum analyzer (PSA-6000, EdCo, Korea), LCR meter (EDC-1630, EdCo, Korea), and digital multimeter (Agilent 34411A), whereas for the control of the ambiental electromagnetic noise and distribution of static voltage we used the TRIFIELD EMF meter (model TF2) and the surface dc voltmeter SVM2 (AlphaLab, USA).

### B. Barkhausen noise recordings

In this paper, we present the results of the BN measurements performed on a  $16 \text{ cm} \times 1 \text{ cm} \times 40 \mu\text{m}$  sample of VITROPERM 800 R supplied from Vacuumschmelze, Germany. VITROPERM 800 R [47] is a commercial nanocrystalline ferromagnetic alloy (82.8 Fe%, 1.3% Cu, 5.6% Nb, 8.8% Si, and 1.5% B by weight) with crystal grains of diameter between approximately 10–15 nm surrounded by an amorphous nonmagnetic residual phase. It has 1.24 T saturation magnetic polarization reached at the field strength above approximately 500 A/m, very high (up to 600 000) treatment-dependent initial susceptibility, negligible magnetostriction, and  $600^\circ\text{C}$  Curie temperature. This sample was annealed for 12 h at  $300^\circ\text{C}$  without a magnetic field.

The Barkhausen noise recordings were performed in the vertically oriented external magnetic field  $H$  parallel to the sample's longest side, which varied in time between  $-550 \text{ A/m}$  and  $550 \text{ A/m}$  according to a periodic zero-mean triangle time profile at 0.5, 1, 2, 5, 10, 20, and 50 mHz frequencies. For each frequency (0.5–10 mHz)/(20–50 mHz), the presented data are measured in the 10–20 V voltage span during 20 field cycles preceded by 50 cycles to reach a closed hysteresis loop. The measurements were performed in the continuous acquisition mode of the Odyssey XE data acquisition system at the 200 kSa/s sampling rate with 16-bit resolution and turned on the internal antialias (low-pass) analog filter at 100-kHz cutoff frequency. The recorded data were stored in a 36 GB internal Odyssey XE acquisition SCSI hard disk, and after completion of measurements transferred to a hard disk of an

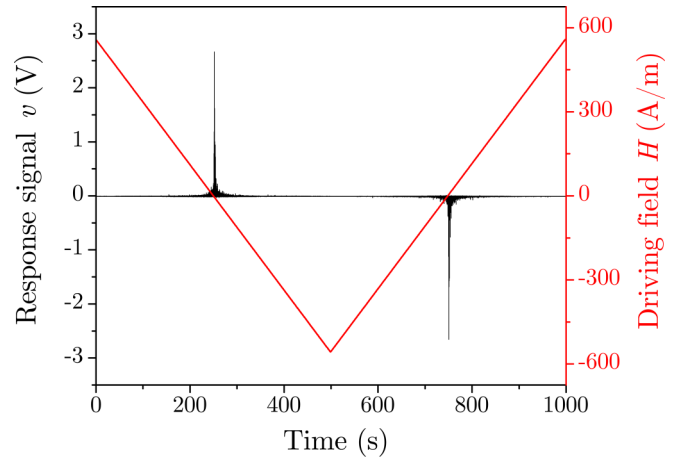


FIG. 2. Time profiles of the response voltage signal  $v$  and the external magnetic field  $H$  (straight line) driving the sample at the 1 mHz frequency shown during one period. In our BN measurements, we connected the pickup coil so that the response signal had the polarity opposite to the sign of  $dH/dt$  in agreement with the Faraday-Lenz's law.

external PC connected to Odyssey for the purpose of storage and numerical processing. All measurements were performed during weekend nights to minimize the amount of external (environmental and electric network) noise.

## III. RESULTS

### A. Experimental BN: Response signal, hysteresis loops, and decomposition of BN signal into BN pulses

In Fig. 2 we illustrate the time profiles of the response signal and the external magnetic field recorded at 1 mHz driving frequency during one period. Examples of time profiles of response signals recorded in one half-period for each of the employed driving frequencies are shown in the main panels of Fig. 3 for 0.5–2 mHz (5–50 mHz) on the left (right) main panel, together with the corresponding hysteresis loops presented in the right insets. Short excerpts of the response signal voltage, recorded around the maximum value of  $H$  when the sample is saturated, show in top-left insets the overall noise of the measurement system and the sample at  $\Omega = 0.5 \text{ mHz}$  (in the left main panel) and  $\Omega = 50 \text{ mHz}$  (in the right main panel). As illustrated by noise histograms in the bottom-left insets, this noise is of the Gaussian type with a standard deviation of less than 5 mV at these two and likewise for the remaining frequencies, so the signal-to-noise ratio by amplitude was maintained above 1000.

As a part of the overall response signal, the pure BN signal arises due to the motion of the domain walls caused by flipping of magnetic moments tending to align with the local effective magnetic field. In ferromagnetic samples, this local field increases or decreases (almost everywhere) together with the external magnetic field, and therefore the corresponding values of induced electromotive force (EMF) are (almost always) one-sided. The domain-wall motion proceeds in the form of one or several avalanches of finite duration possibly merging in time and space. Each such event induces a BN

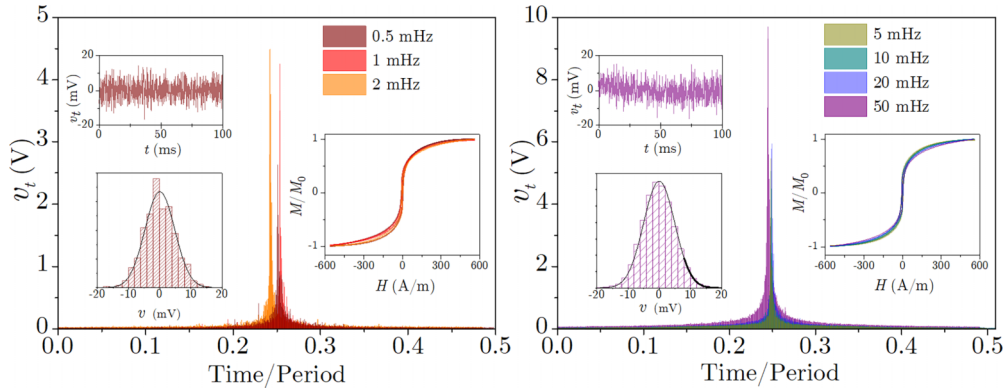


FIG. 3. Main panels show one example of time profiles of the voltage response signal  $v_t$  recorded during a single half-period of the external driving field  $H$  for each of the employed “slow” (left) and “fast” (right) driving frequencies  $\Omega$  quoted in legends. Top-left inset in the left main panel presents an excerpt of the time profile of the response signal recorded at  $\Omega = 0.5$  mHz near the maximum value of the external field  $H$ , while the histogram of presented values illustrates in the bottom-left inset of the same panel that these values are normally distributed, which could be mainly attributed to random fluctuations of sample’s magnetization. In the right panel, the left insets show the same, but for  $\Omega = 50$  mHz, while for the remaining frequencies, the corresponding distributions are roughly the same with the standard deviation less than 5 mV. Hysteresis curves, displaying versus the external magnetic field  $H$  the sample’s magnetization  $M$  scaled by maximum magnetization  $M_0$ , are given in the right insets.

pulse—a sequence of nonzero pure BN signal values of the same sign realized in contiguous short intervals of time.

Figure 4 shows a part of the recorded signal suggesting that the response signal can be considered as a train of BN pulses, separated in time by the inactivity intervals of the sample during which the pure BN signal is absent. This means that the recorded signal can be decomposed into BN pulses, which is, however, not straightforward due to the superimposed induced voltage caused not by the rearrangements of the magnetic domains but by other means. Indeed, some EMF is induced in the pickup coil because of the varying external magnetic field even without inserted sample. For the noiseless triangle

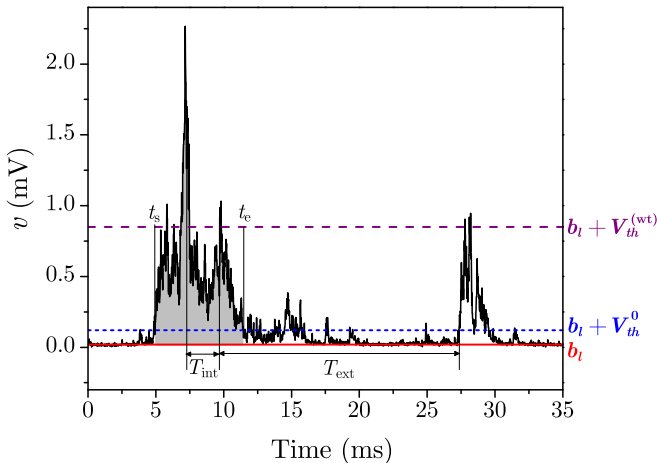


FIG. 4. Part of the time-profile of the response signal  $v$  and horizontal lines representing (bottom to top): The baseline  $b_l$  (full line), base threshold level  $b_l + V_{th}^0$  (dotted line), and waiting-time threshold level  $b_l + V_{th}^{(wt)}$  (dashed line). Base threshold  $V_{th}^0$  is used in the decomposition of the response signal into BN pulses (one such pulse, starting at  $t_s$  and ending at  $t_e$ , is shaded in gray), while the waiting-time threshold  $V_{th}^{(wt)}$  is used in the analysis of waiting times (e.g., internal and external waiting time,  $T_{int}$  and  $T_{ext}$ ).

time profile of the driving field, this contribution would appear in the signal time profile as a horizontal line switching its level at the half-period transitions, whereas in reality some concomitant noise, caused by all factors except the change of sample’s magnetization and therefore *external*, is inevitably superimposed as well. Due to this, several methods for baseline determination in the presence of noise (and investigated signal, here pure BN) have been proposed so far; see, e.g., Refs. [48,49]. Here, like in Ref. [4], we used the simplest and the fastest one in which the baseline level  $b_l$  is taken so that it corresponds to the discrete value of the digitized signal that is most frequently visited during the ongoing half-period, cf. Fig. 4.

The next step in the decomposition of the recorded signal into BN pulses is the establishment of some threshold region around the baseline and subsequent recognition of the recorded signal parts lying outside that region as BN pulses. Here the threshold region is taken as the range of signal values  $v$  satisfying  $b_l - V_{th} < v < b_l + V_{th}$  for some chosen threshold  $V_{th} > 0$ . As for the signal value  $v$  close to  $b_l$  one cannot resolve whether the external noise dominantly causes its part  $v - b_l$  or not, the purpose of  $V_{th}$  is to discriminate between these two cases. So for  $|v - b_l| < V_{th}$  (and small enough  $V_{th} > 0$ ), one can consider that  $v$  is dominantly caused by other (i.e., non-BN) causes and disregard such signal points from further analysis of BN distributions, whereas the remaining part of the recorded signal, despite being polluted by the external noise, is taken as the BN signal relative to the baseline and proceeded to further analysis. For the threshold  $V_{th}$  used in the foregoing way we say that it plays the role of a *base* threshold, in which case we will denote it as  $V_{th}^0$ .

The so-obtained BN signal is already decomposed into BN pulses, each being a subsequence,

$$\{v(t_s), v(t_s + \Delta t), \dots, v(t_e)\},$$

of the overall recorded sequence of digitized signal values  $v(t)$  taken in the interval  $\{t_s, t_s + \Delta t, \dots, t_e\}$  of contiguous discrete moments of acquisition time starting at  $t_s$  and ending at  $n\Delta t$



later moment  $t_e$ , where  $\Delta t$  is the sampling interval ( $= 5 \times 10^{-5}$  s in our case), cf. Fig. 3.  $t_s$  and  $t_e$  are defined in the usual way such that for a positive BN burst the signal goes above the threshold at  $t = t_s$  and stays above the threshold until  $t = t_e$ , when it goes below the threshold for the first time after the start of the burst; note that for negative bursts, the opposite applies (i.e., the event starts at  $t = t_s$ , when the signal goes below the negative threshold and lasts until it goes above it at  $t = t_e$ ). Each BN pulse of a ferromagnetic sample is either positive or negative, i.e., all its values are either above  $b_l + V_{\text{th}}^0$  or below  $b_l - V_{\text{th}}^0$ , depending on the sign of  $dH/dt$ , cf. Fig. 2.

The collection of BN pulses extracted via the foregoing procedure from the overall recorded signal depends on the choice of threshold  $V_{\text{th}}$ . Because the basic role of imposing a threshold is to keep in further analysis most of the data points that are likely caused by BN reasons, a natural way would be to choose a threshold taking into account the width  $w$  of the external noise. As explained in Ref. [4], this width can be estimated from the data lying below the baseline and take  $V_{\text{th}}^0$  proportional to this width,  $V_{\text{th}}^0 = d_l w$ , using reasonable discrimination levels  $d_l$  (e.g., between 0.5 and 3). Alternatively, the base threshold can be chosen differently, e.g., fixed to some constant value approximately matching the width of external noise, as we did in this paper.

Besides playing the role of a base threshold that is used in the decomposition of the response signal into BN pulses, variable threshold values are used in the analysis of waiting times (see the next subsection) in which case such threshold will be referred to as the waiting-time threshold  $V_{\text{th}}^{(\text{wt})}$ . The logic here is to first define a pulse with one threshold ( $V_{\text{th}}^0$ ) and then a new threshold with another value ( $V_{\text{th}}^{(\text{wt})}$ ) in order to be able to classify the waiting times into internal (due to breaking of the bursts into subavalanches) and external ones (those separating the “original” bursts) [50].

### B. Experimental BN distributions

Each BN pulse  $\{v(t_s), v(t_s + \Delta t), \dots, v(t_e)\}$  is characterized by several parameters. Mostly analyzed are its size

$$S = \sum_{k=0}^n [v(t_s + k\Delta t) - b_l] \Delta t ;$$

duration

$$T = t_e - t_s,$$

i.e., the time interval between its ending moment  $t_e$  and starting moment  $t_s$ ; energy

$$E = \sum_{k=0}^n [v(t_s + k\Delta t) - b_l]^2 \Delta t ;$$

and amplitude

$$A = \max\{v(t_s) - b_l, \dots, v(t_e) - b_l\} .$$

Regarding the question of to what extent are the so-obtained parameter values affected by the external noise, one can take that while the width of (zero-mean) noise is comparatively small and its values uncorrelated, it cannot affect much the individual parameter values for moderate and large BN pulses and likely has no effect on their statistics.

In Fig. 5 are presented the log-log plots of the experimental probability density functions (i.e., distributions with the unit area at the lin-lin scale) of size  $S$ , duration  $T$ , energy  $E$ , and amplitude  $A$  of BN pulses. Presented are the integrated distributions, i.e., the distributions extracted along the entire hysteresis loop, which correspond to six values of base threshold  $V_{\text{th}}^0$  from the signals recorded at 5 mHz.

Previous studies of Barkhausen noise emissions (see, e.g., Refs. [4,51]) and our data from Fig. 5 show that these distributions follow the (modified) power laws,

$$D_X(X) = \mathcal{D}_X(X/X_0, X/X_1, \dots)/X^{\alpha_X}, \quad (1)$$

where  $X$  denotes one of the avalanche parameters (size  $S$ , duration  $T$ , energy  $E$ , and amplitude  $A$ ) and  $\alpha_X$  the pertaining power-law exponent ( $\tau$ ,  $\alpha$ ,  $\varepsilon$ , and  $\mu$  for  $X = S, T, E, A$ , respectively). The exponents are associated with the slope of the log-log plot of  $D_X(X)$  in its scaling region (i.e., the part in which this plot appears as linear), while the cutoff function  $\mathcal{D}_X(X/X_0, X/X_1, \dots)$ , depending on the cutoff parameters  $X_0, X_1, \dots$ , describes the departure of  $D_X(X)$  from the power-law shape at the distribution ends (e.g.,  $\mathcal{D}_X(X/X_l, X/X_u) \approx \text{const}$  for  $X_l \leq X \leq X_u$  for the cutoff function specified by the lower cutoff  $X_l$  and the upper cutoff  $X_u$ ).

The data displayed in Fig. 5 show that, although the choice of base threshold affects the shape of distributions, they all exhibit scaling regions which seem to be visually approximately parallel in their main part. This we quantified by extracting the effective values of the corresponding exponents (by the simple linear fit applied in the main part of the scaling region for each of them; see the comment [52]) and presenting their variation with the chosen base threshold  $V_{\text{th}}^0$  in the inset for each of the distributions. Except for the energy exponent  $\varepsilon$ , the so-obtained exponent values are not constant but instead show a systematic change with  $V_{\text{th}}^0$  maintaining (within the uncertainty bars) the fulfillment of the scaling relations [4,53,54]:

$$\tau = 1 + (\alpha - 1)/\gamma_{S/T}, \quad (2)$$

$$\varepsilon = 1 + (\alpha - 1)/(2\gamma_{S/T} - 1), \quad (3)$$

$$\mu = 1 + (\tau - 1)/(1 - 1/\gamma_{S/T}), \quad (4)$$

containing the exponent  $\gamma_{S/T}$ , see Eq. (5), whose variation with  $V_{\text{th}}^0$  is shown in the left panel of Fig. 10.

Regarding the choice of the base threshold values employed in Fig. 5, we notice that, due to 5-mV noise width, the value of 1-mV base threshold is too small, enabling some signal parts dominated by the external noise to be recognized as (small) BN pulses, and also an occasional artificial merging of several separate BN pulses lined up in a sequence into larger ones. The next two values of  $V_{\text{th}}^0$ , namely 10 and 20 mV, should be the most appropriate at the current (i.e., 5 mV) noise width because they statistically eliminate the influence of external noise and do not discriminate recognition of BN pulses that are not too small. The distributions extracted at these two  $V_{\text{th}}^0$  values indicate the existence of two scaling regions like the ones observed in the case of the RFIM avalanche distributions of thin systems; see Refs. [55–58]. There it was shown that the small avalanches, not reaching the system borders, propagate like in bulky 3D systems, whereas the big avalanches effectively propagate like 2D avalanches being

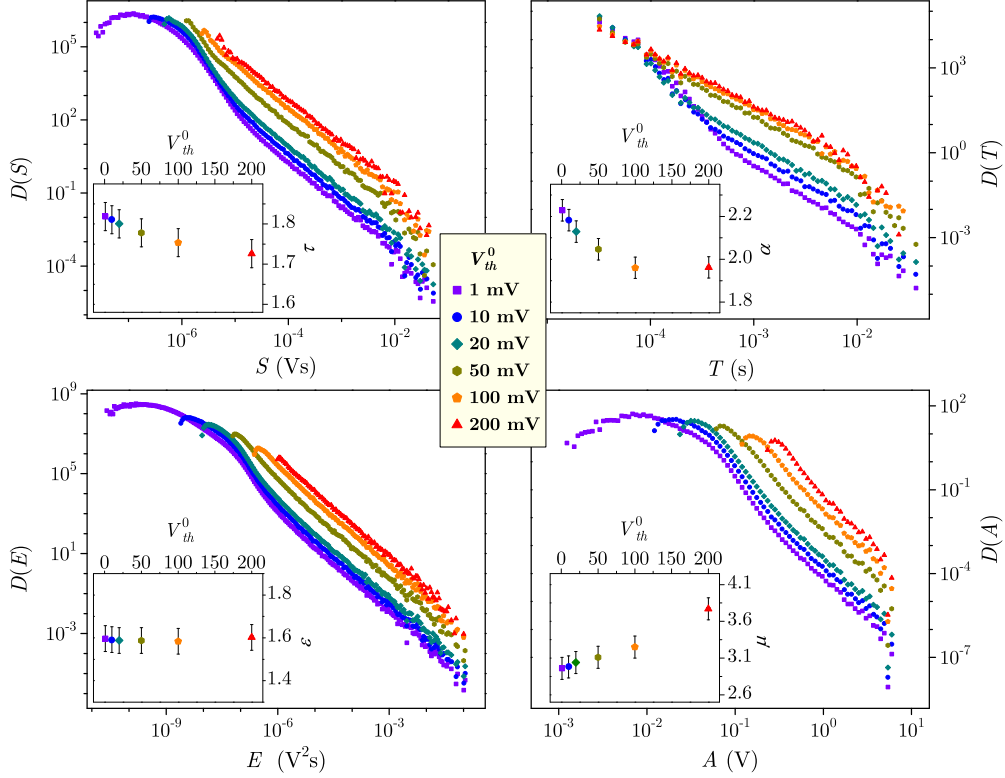


FIG. 5. For the values of base threshold  $V_{th}^0$  quoted in the (common) legend, we give in main panels the integrated distributions of size  $S$ , duration  $T$ , energy  $E$ , and amplitude  $A$  of BN pulses all collected from the data recorded in 20 cycles of the external magnetic field at the same driving rate  $\Omega = 5$  mHz. All distributions are normalized to the unit area at the lin-lin scale so as to be the experimental probability density functions. In the insets, we show the variation with  $V_{th}^0$  of the effective values of the distributions' exponents [ $\tau$  for  $D(S)$ ,  $\alpha$  for  $D(T)$ ,  $\varepsilon$  for  $D(E)$ , and  $\mu$  for  $D(A)$ ] with the error bars mainly caused by the variation of the fitting region.

sandwiched between the top and bottom system boundaries. So the small 3D-like avalanches dominate in the initial steeper scaling region, followed by the less steep one caused by the big 2D-like avalanches. The initial (i.e., 3D-like and steeper) part of the distributions' scaling region gradually vanishes with further increase of  $V_{th}^0$  and the distributions attain the shape of a single-slope power law sharply decreasing at the large avalanche end.

Experimental BN studies performed so far revealed that between the duration  $T$  and the average size  $\langle S \rangle_T$  of BN pulses of duration  $T$  should exist the correlation of a power-law type

$$\langle S \rangle_T \sim T^{\gamma_{S/T}}, \quad (5)$$

specified by the power-law exponent  $\gamma_{S/T}$ . Our 5-mHz data from the top panel of Fig. 6 suggest that the experimental value of this exponent, determined from the slope of the scaling region in its large-avalanche (linear) part, slightly depends on the choice of base threshold as is visible in the figure. Moreover, our data for  $V_{th}^0 < 50$  mV indicate the presence of two scaling parts in graphs. The initial one shows the correlations between  $\langle S \rangle_T$  and  $T$  for small avalanches and continues through a transitional region to the main part of the scaling region giving the correlations for larger avalanches.

The BN power spectrum  $P(f)$ , i.e., the (spectral) density of power released by the BN signal at frequency  $f$ , is expected

to follow the power law

$$P(f) \sim f^{-\gamma_{\text{spc}}}, \quad (6)$$

specified by the power exponent  $\gamma_{\text{spc}}$ . In experiments, the BN signal is polluted by the external noise, so that the experimental power spectrum deviates from the power law most notably at the higher frequencies at which the noise dominates the Fourier components of the BN signal. This is noticeable in the experimental power spectra, exemplified in the bottom panel of Fig. 6 by the integral spectra recorded at three driving rates (0.5, 5, and 50 mHz) along the entire hysteresis loop (and shown by the pale lines). The clearest example is the 0.5 mHz integral spectrum whose power-law part is absent due to the proportionally longest interval of time virtually without the BN noise. As the driving rate increases, the interval with a pronounced BN signal gets proportionally longer, as does the power-law spectrum part. To reduce the influence of noise, we also calculated the binned power spectra, i.e., the power spectrum of the response signal recorded in a narrow window of the external magnetic field centered at that value of  $H$  at which the averaged response signal attains its maximum. Under our experimental conditions, the binned spectra seem to be only weakly polluted by the external noise up  $\sim 20$  kHz, so their power-law part extends that far.

As previously mentioned, thresholds are also used in the analysis of waiting times which are defined in the following way. For any threshold  $V_{th}^{(wt)}$ , chosen for the waiting-time analysis, some parts of the response signal remain below the

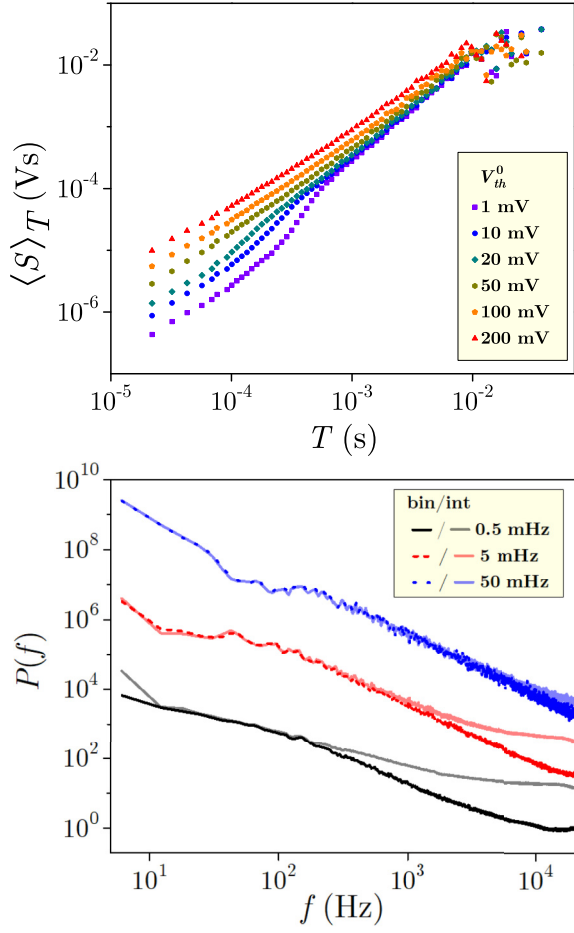


FIG. 6. Top panel: Correlations between duration  $T$  and the average size  $\langle S \rangle_T$  of BN pulses with duration  $T$  obtained for the same values of base threshold  $V_{th}^0$  as in Fig. 5. Bottom panel: BN power spectra  $P(f)$  against frequency  $f$  collected at three driving rates (0.5, 5, and 50 mHz) along the entire hysteresis loop (int) and in a narrow window (bin) of the external magnetic field centered at the maximum of the average response signal. For both panels, the underlying sets of experimental data are the same as in Fig. 5.

imposed waiting-time threshold level  $b_l + V_{th}^{(wt)}$ , meaning that at any moment  $t$  in such part  $v(t) < b_l + V_{th}^{(wt)}$ . The start  $t_s$  and end  $t_e$  of each of the corresponding intervals of time are (figuratively speaking) determined by two successive intersections of the response signal with the waiting-time threshold level, see in Fig. 4. So one can take the duration  $T_w = t_e - t_s$  between these two moments  $t_s$  and  $t_e$  as the *waiting time* and classify it either as the *external* waiting time  $T_{ext}$  or *internal* waiting time  $T_{int}$  if the moments  $t_s$  and  $t_e$  belong to different or same activity event, respectively.

In Fig. 7, we present three types of distributions of waiting time: Total waiting time  $T_w$  in the top panel, external waiting time  $T_{ext}$  in the middle panel, and internal waiting time  $T_{int}$  in the bottom panel. These distributions become of a power-law type for the sufficiently high values of waiting-time threshold  $V_{th}^{(wt)}$  signifying the presence of temporal correlations; otherwise, they are exponential, showcasing the random waiting times and absence of temporal correlations.

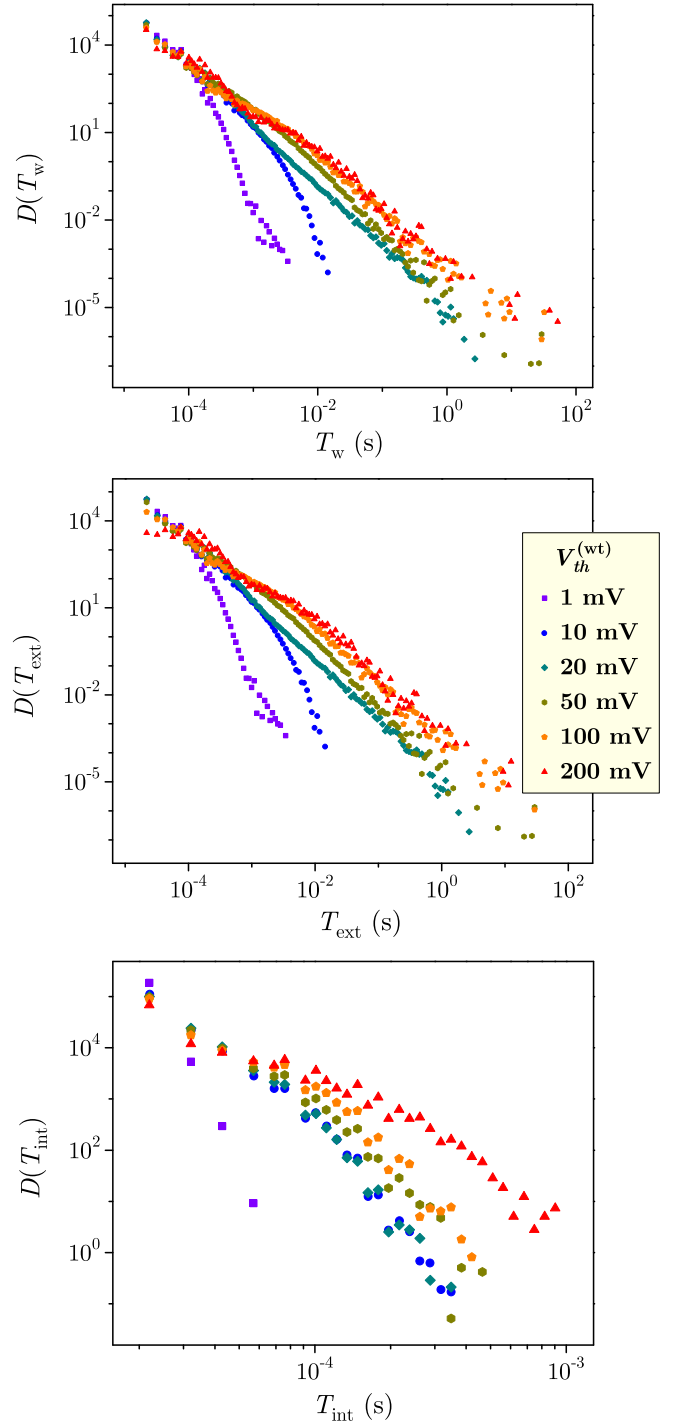


FIG. 7. Distributions of various types of waiting times: Total  $T_w$  in the top, external  $T_{ext}$  in the middle, and internal  $T_{int}$  in the bottom panel. The distributions are obtained at the 5 mHz driving frequency for the same threshold levels and the same sets of data as in Fig. 5.

### C. Comparison with RFIM

In this section, we compare our experimental results with the results of numerical simulations of the athermal nonequilibrium random field Ising model [36,39] driven at finite rates with the aim to test its suitability for interpretation of the behavior of field-driven disordered nanocrystalline

ferromagnets; see more in Appendix B. Since at room-temperature conditions, like in our experiment, thermal fluctuations in real systems should not be important, we employed the athermal (i.e., zero-temperature) model version [37–39] which is significantly less demanding than the thermal (i.e., finite-temperature) version. In the athermal version the distribution of the random field is quenched and therefore the model behavior is fully deterministic, meaning that driving the system through the next hysteresis cycle gives the same results. This is not consistent with BN experiments having a somewhat different response in repeated hysteresis cycles that might originate, e.g., from thermal noise and/or redistribution of stress within the sample from cycle to cycle. To overcome this deficiency, simulations are performed using a different configuration of the random field in each run, and the so-obtained results are averaged over employed configurations having all the same value of the disorder parameter (this is known as quenched averaging).

### 1. On the model and numerical simulations

In the RFIM,  $N$  Ising spins  $s_i = \pm 1$ , located at the sites  $i$  of a lattice, interact with their nearest neighbors ferromagnetically and are exposed to a homogeneous external magnetic field  $H$  like in the Ising model. Additionally, in the random field variant of the Ising model, the spins are also influenced by a quenched random magnetic field taking uncorrelated values  $h_i$  at lattice sites  $i$  from a zero-centered Gaussian (i.e., normal) distribution,

$$\rho(h_i) = \frac{\exp[-h_i^2/2R^2]}{\sqrt{2\pi}R}, \quad (7)$$

whose standard deviation  $R$  is taken in the RFIM as the parameter measuring disorder in the system. In this way, the averages  $\langle h_i \rangle_R$  and  $\langle h_i h_j \rangle_R$  corresponding to (all) possible random field configurations at disorder  $R$  satisfy

$$\langle h_i \rangle_R = 0, \quad \langle h_i h_j \rangle_R = \begin{cases} R^2, & \text{if } i = j \\ 0, & \text{otherwise} \end{cases}. \quad (8)$$

In the athermal nonequilibrium RFIM version, employed in this work, the evolution of the system is determined by the driving protocol and by the following dynamical rule:

*the spin  $s_i$  is **unstable** at the moment  $t_m$  and **will flip** at the next moment of time  $t_m + \Delta t_m$  if*

$$h_i^{\text{eff}}(t_m) s_i(t_m) < 0;$$

*otherwise,  $s_i$  is **stable** at the moment  $t_m$  and **will retain** its value at the next moment.*

Here,

$$h_i^{\text{eff}}(t_m) = \sum_j s_j^{(i)}(t_m) + H(t_m) + h_i, \quad (9)$$

is the (local) *effective field* acting on  $s_i$  at the moment  $t_m$  of discrete time and  $\Delta t_m = 1$ . The effective field  $h_i^{\text{eff}}(t_m)$  is the sum of the random field  $h_i$  at site  $i$ , (homogeneous) external magnetic field  $H(t_m)$  at the moment  $t_m$ , and the term  $\sum_j s_j^{(i)}(t_m)$  giving the influence on  $s_i$  at the moment  $t_m$  of its nearest neighbors  $s_j^{(i)}$ . The flipping of unstable spins reduces

the value of the system Hamiltonian

$$\mathcal{H} = - \sum_{(ij)} s_i s_j - H \sum_i s_i - \sum_i h_i s_i, \quad (10)$$

and spreads like an avalanche until all spins in the system become stable. When all spins are stable the system is in a stationary state which is not necessarily the equilibrium one (i.e., the state of minimum energy at the current value of the external magnetic field  $H$ ) but will be maintained until destabilized by some change in the external magnetic field  $H$ .

In the *adiabatic* driving of the athermal nonequilibrium RFIM [39,59] each avalanche is nucleated due to such change in the external magnetic field  $H$  that destabilizes only the least stable spin; thereafter,  $H$  is kept constant as long as the nucleated avalanche lasts propagating over the shell of the nearest neighbors of spins flipped at the previous moment, the shell being placed at the rim of the cluster of spins flipped during the ongoing avalanche.  $H$  is also kept constant during each avalanche in the *quasistatic* driving of the model and repeatedly changed by a fixed amount  $\Delta H$  while the state of the system is stationary. This type of driving is therefore suitable for simulations of systems having two timescales, namely an internal timescale that is much faster than the timescale at which  $H$  changes.

On the other hand, in the *finite driving rate* protocol, the external magnetic field  $H$  changes in each time step by some constant increment  $\Delta H$ , i.e., at the driving rate  $\Omega = \Delta H / \Delta t_m$ , facilitating the propagation of the ongoing avalanche(s). Like for the quasistatic driving, such driving occasionally causes the simultaneous nucleation of several avalanches when  $\Delta H$  and/or lattice size are large, and/or the nucleation of new avalanche(s) while the ongoing avalanche is still active [60–63]. These separately nucleated avalanches may overlap in time (and possibly merge in space) forming a single activity event [64]. The activity events are separated in time by the intervals of the system's inactivity, leading in this model version to the natural choice of baseline level  $b_i = 0$  and identification of the event parameters (size  $S$ , duration  $T$ , energy  $E$ , and amplitude  $A$ ) like in the experimental case, but after setting the value of base threshold in simulations to  $V_{\text{th}}^0 = 1$ .

Because of the symmetry between the rising and falling part of the hysteresis loop, we performed the numerical RFIM simulations only along the rising part by the field  $H(t)$  increasing at a constant driving rate  $\Omega$  like in our experiments. Each simulation starts with all spins set to  $-1$  and some concordant big negative value of  $H$ , and afterward,  $H$  is increased until all the spins are flipped to 1. We performed the simulations with the aid of the so-called sorted list algorithm (see in Refs. [53,65]) modified and adjusted for the finite-rate driving protocol.

Unlike in the athermal RFIM version, where quasistatic and finite rate driving reduce in  $\Delta H \rightarrow 0$  limit to adiabatic, nonequilibrium stationary states are absent in the thermal RFIM version because of the nonzero probability  $p_i = [1 + \exp(-2s_i h_i^{\text{eff}}/T)]^{-1}$  of thermal flipping of (any chosen) spin  $s_i$  in the effective field  $h_i^{\text{eff}}$  at temperature  $T$ . This causes thermal fluctuations of average magnetization  $M = (\sum_i s_i)/N$  tending to drive the system towards the equilibrium state at



the current value of the external magnetic field  $H$  in the spirit of Glauber model [66]. We note that the thermal effects can be neglected because of the high Curie temperature ( $600^\circ\text{C}$ ) of the VITROPERM 800 R sample and the experiments performed at room temperature. Therefore, the above-described formulation of the thermal RFIM, as well as other possible generalizations of thermal spin models (e.g., Kawasaki model [67] and Swendsen-Wang model [68]) for the RFIM will not be considered in this work.

## 2. Comparison of results of experimental BN measurements and numerical simulations of RFIM

In order to optimally match the simulation results to experimental, one can adjust in simulations the shape and size of the lattice, the value of disorder  $R$ , and the value of driving rate  $\Omega$ . To this end, we performed simulations using the  $32\,768 \times 2048 \times 8$  striplike cubic lattice with open boundaries mimicking our experimental samples by the ratio of its sides.

Next, because of unknown value of disorder which might provide results similar to the experimental, we performed simulations for several values representing all three domains of disorder for the employed lattice (below critical, transitional, and above critical, see in Ref. [59]), and for each of them at a set of values of  $\Omega$  from  $10^{-10}$  to  $10^{-6}$  covering for this lattice all types of driving regimes from slow (without spanning events [69,70]) to fast (large spanning events of quasi-2D type [71]), see in Refs. [62,64].

For each pair of simulation parameters ( $R, \Omega$ ) we performed 20 simulations with different realizations of the random magnetic field. As the activity events in simulations are clearly extraditable as the longest subsequences of the nonzero values appearing in the (noiseless) response signal at contiguous moments of time, the collecting of their statistics would be natural to perform with the base threshold  $V_{\text{th}}^0 = 1$ . Still, for the intended comparison with experiments, we did this for all distributions at the same base threshold  $V_{\text{th}}^{\text{sim}} = 5$  in simulations and at the same base threshold in experiments  $V_{\text{th}}^{\text{exp}} = 50$  mV. Despite the fact that the  $(V_{\text{th}}^{\text{exp}}, V_{\text{th}}^{\text{sim}})$  pairs, chosen individually for each pair of the compared distributions, would provide closer matching, for simplicity we decided to perform all comparisons using the above pair of fixed thresholds with a remark that at and above  $V_{\text{th}}^{\text{exp}} = 50$  mV the  $\langle S \rangle_T - T$  experimental correlations have the scaling region with a single slope, cf. Fig. 6, and that for  $V_{\text{th}}^{\text{sim}} = 5$  and all employed rates the ratio (rms of simulation signal): $V_{\text{th}}^{\text{sim}}$  is roughly the same as in experiment at  $V_{\text{th}}^{\text{exp}} = 50$  mV.

In Fig. 8 we compare the integrated distributions of avalanche event parameters (size, duration, energy, and amplitude) collected along the entire hysteresis loops in our experimental measurements and in numerical simulations. The presented simulational distributions are obtained for disorder  $R = 2.3$ , being above the effective critical disorder for the adiabatically driven  $32\,768 \times 2048 \times 8$  RFIM system [58], and at a set of “nice” values of the driving rate quoted in legend chosen in the same progression as the experimental ones. Among the tested driving rates and disorder values, ranging between  $R = 1.8$  and  $R = 3.0$  in 0.1 increments, this combination of driving rates and disorder provided the best

achieved matching between experimental and simulational distributions presented in this and all subsequent figures.

Because of the different time and signal scales in the experiment and in simulations (real scales in the experiment and discrete model scales in simulations), the matching of the two is achieved by dividing the simulational timescale by the factor  $c_t = 2 \times 10^5$  (equal to the sampling rate used in our experiment) and the signal scale by the factor  $c_v = 50$  (hence, the factor  $c_t c_v = 10^7$  for the scale of avalanche size and the factor  $c_t c_v^2 = 5 \times 10^8$  for the scale of avalanche energy) providing the best matching with the experimental distributions. In addition to this, due to the existing difference in both the shape and the logarithmic span, the distributions obtained from the simulations are shifted along the vertical axis so to attain the best overlapping in the scaling regions of the pairing distributions obtained in the experiment.

The data presented in Fig. 8 show a significant overlapping for the pairs of distributions at faster rates and overlapping in the scaling region but noticeable discrepancies in the initial and final part of the distributions at slower rates. The overlapping is the least in the case of amplitude distributions which could be related to a significantly smaller dynamic range of the simulated response signal at the chosen lattice size. Comparison between the experimental and simulational  $\langle S \rangle_T - T$  correlations, presented in the left panel of Fig. 9, is performed for the same sets of experimental and simulational data as in Fig. 8 using the same  $c_t$  and  $c_t c_v$  factors and the same threshold pairs. The best overlapping is obtained between 1 mHz ( $1 \times 10^{-8}$ ) and 2 mHz ( $2 \times 10^{-8}$ ) experimental (simulational) driving rates, while for higher rates the experimental correlations depart more and more from the power law, likely due to spatial merging of avalanches occurring at these rates.

Even more intricate is the behavior of power spectra. Comparison of the experimental and simulational binned spectra for the used experimental (simulational) driving rates is shown in the right panel of Fig. 9. The compared data suggest that the experimental BN (binned) spectra can be described by the power law

$$P(f) \sim f^{-\gamma_{S/T}}, \quad (11)$$

meaning that the power exponents  $\gamma_{\text{spc}}$  and  $\gamma_{S/T}$  might be the same, as it was suggested in Ref. [72] within the RFIM context. Here, however, one must take into account that both experimental and simulational effective values of the exponent  $\gamma_{S/T}$  depend on the choice of the imposed base threshold  $V_{\text{th}}^0$  and on the driving rate  $\Omega$ , which we illustrated in Fig. 10. The data displayed in this figure show that both  $\gamma_{\text{spc}}$  and  $\gamma_{S/T}$  vary with threshold  $V_{\text{th}}^0$  in a similar way decreasing from their maximum values at zero base threshold towards values at a plateau, one in the experimental and the other ( $\sim 0.1$  lower) in the simulational case, attained at rather high base thresholds. For each fixed value of base threshold  $V_{\text{th}}^0$ , the variation of  $\gamma_{S/T}$  with  $\Omega$  is less, but present, including the plateau values. On the other hand, the effective values of  $\gamma_{\text{spc}}$  for different  $\Omega$ , displayed in the insets of these main panels, seem to be the same in the experimental case as the corresponding values of  $\gamma_0$  (i.e., the effective value of  $\gamma_{S/T}$  for the smallest base threshold  $V_{\text{th}}^0$  at the current driving rate  $\Omega$ ), but not in the simulational case except for the very small driving rates. However, in both

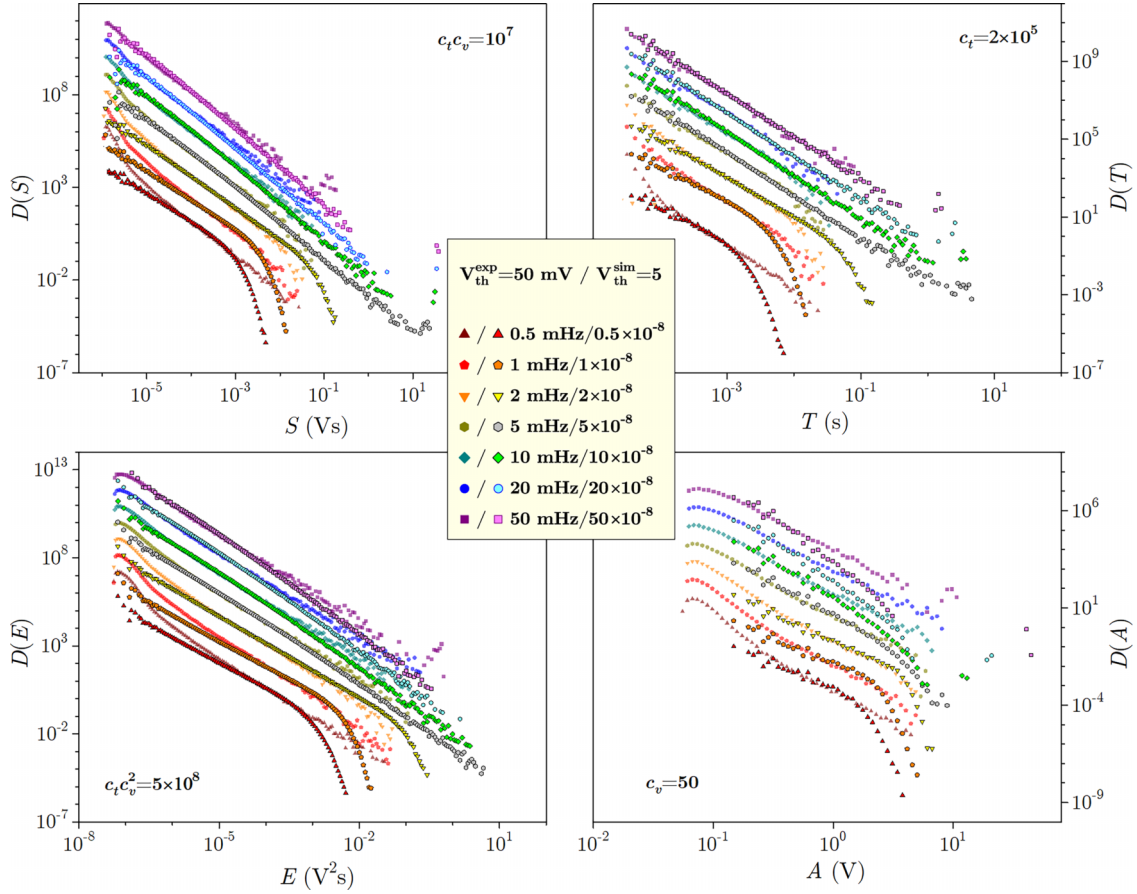


FIG. 8. Comparison of integrated (unit area) distributions of avalanche parameters (size  $S$ , duration  $T$ , energy  $E$ , and amplitude  $A$ ) obtained in experiments and numerical RFIM simulations for the experimental (simulational) driving rates quoted in the common legend. Each experimental distribution is extracted at the (same) experimental base threshold  $V_{th}^{exp} = 50$  mV of 20 hysteresis cycles data and presented with full symbols on the requisite scale using SI units for time and voltage. Starting from the distribution recorded at the lowest driving rate, each experimental distribution obtained at the next (higher) rate is for better visibility vertically translated by one decade upwards relative to the distribution recorded at the previous (lower) rate. Each simulational distribution is extracted at the (same) simulational base threshold  $V_{th}^{sim} = 5$  of 20 RFIM simulations on the  $32\,768 \times 2048 \times 8$  cubic lattice performed with different realizations of the random magnetic field with disorder  $R = 2.3$ . For comparison, the simulational distributions, presented by empty symbols, are shifted along the horizontal axis dividing the data by a suitable factor ( $c_t = 2 \times 10^5$  for  $T$  axis,  $c_v = 50$  for  $A$  axis,  $c_t c_v = 1 \times 10^5$  for  $S$  axis, and  $c_t c_v^2 = 5 \times 10^8$  for  $E$  axis).

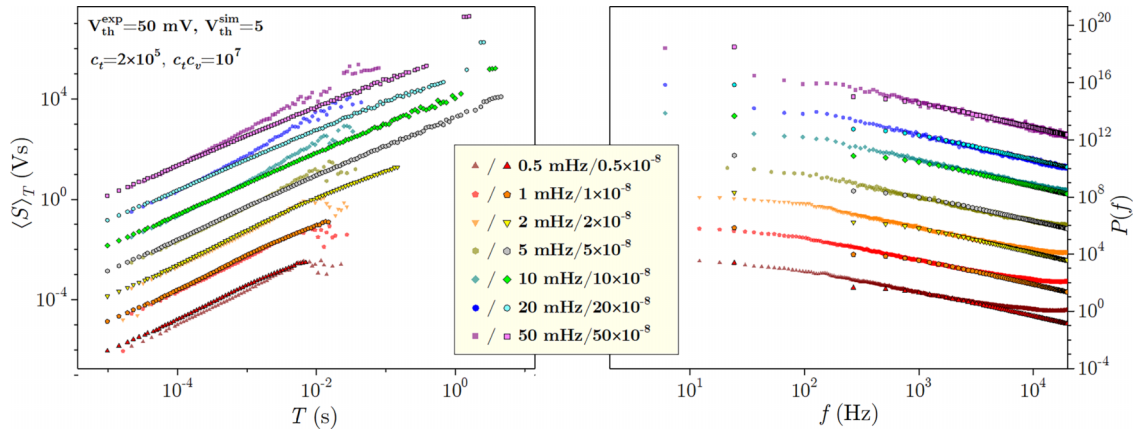


FIG. 9. Left panel: Comparison of the experimental and simulational correlations between the avalanche duration  $T$  and the average avalanche size  $\langle S \rangle_T$  of that duration extracted at the same experimental and simulational base thresholds, the same values of experimental and simulational driving rates, and the same  $c_t$  and  $c_t c_v$  factors as in Fig. 8. Right panel: Comparison of the experimental and simulational power spectra  $P(f)$  for the driving rates from the legend. Simulational frequencies are multiplied by the factor  $c_t = 2 \times 10^5$ . For visibility, each of the next-driving-rate curves in both panels is shifted vertically upwards by one-two decades in left-right panel relative to the previous one. The underlying sets of data are the same as in Fig. 8.

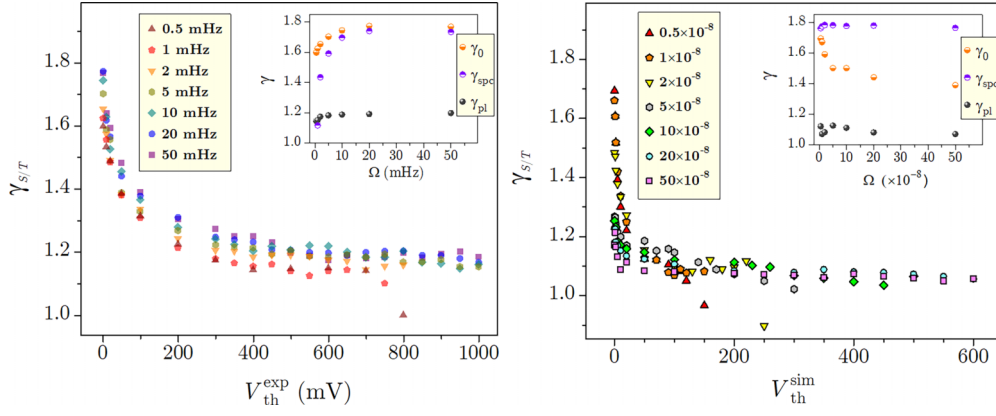


FIG. 10. Left panel: Effective experimental values of the exponent  $\gamma_{S/T}$  against the base threshold  $V_{th}^{exp}$ . In the inset, we show against the driving rate  $\Omega$  the effective experimental values of  $\gamma_0$  (i.e., the value of  $\gamma_{S/T}$  at the current driving rate  $\Omega$  for the smallest experimental base threshold  $V_{th}^{exp} = 1$  mV),  $\gamma_{spc}$  (i.e., power spectrum exponent), and  $\gamma_{pl}$  (i.e., plateau value of the exponent  $\gamma_{S/T}$  at the corresponding driving rate  $\Omega$ ). Right panel: The same as in the left panel but for the values obtained from the simulational data. Each effective exponent value is the slope determined by the linear fit in the power-law region of the corresponding distribution. The underlying data sets and other relevant parameters are the same as in Fig. 8.

experimental and simulational cases, the power exponent  $\gamma_{spc}$  is undoubtedly different for the corresponding plateau values at all driving rates.

In Fig. 11 we compare the distributions of waiting time: Total, external, and internal shown in the top, middle, and bottom panel, respectively. The distributions calculated from the experimental and simulated data are overlapped to a high degree in the whole range of waiting times, except for the distributions of internal waiting times which overlap only in their scaling regions.

The average avalanche shape [74] is given by  $\langle v_t/v_t^{max} \rangle$  (i.e., the average value of the response signal  $v_t$  scaled by its maximum value  $v_t^{max}$  during the avalanche) taken as a function of  $t/T$  (i.e., the time  $t$  measured from the beginning of avalanche scaled by the avalanche duration  $T$ ). Figure 12 shows that both in experiment and simulations these shapes are parabolic-like and rather similar, the experimental being slightly right-skewed and simulational (even less) left-skewed. Performing the fits of the average avalanche shape data to the functional form (found in Ref. [74])

$$\langle V(t|T) \rangle \propto T^{\gamma-1} \left[ \frac{t}{T} \left( 1 - \frac{t}{T} \right) \right]^{\gamma-1} \left[ 1 - a \left( \frac{t}{T} - \frac{1}{2} \right) \right] \quad (12)$$

allows us to estimate exponent  $\gamma$  as the fitting parameter; here parameter  $a$  accounts for the underlying asymmetry of the average avalanche shape. So-estimated values of  $\gamma$  are contrasted to the  $\gamma_{S/T}$  data and are shown in the inset of Fig. 12 against the driving rate  $\Omega$ . One can observe that the values remain fairly close and consistent in the region of low driving rates but begin to vary more and more as the driving rate increases. Two of the representative fits to the function (12) are included in the main panel of Fig. 12, shown with full line.

Finally, in Fig. 13 we contrast the magnetizations and magnetic susceptibilities obtained from the experiment and the numerical simulations. Magnetizations, rescaled by the saturation value  $M_0$  and susceptibilities  $dM/dH$ , are presented against the external magnetic field  $H$ . Regarding the behavior of these curves below and above the coercive field  $H_c$  (i.e., the

value of the external field  $H$  at which  $M = 0$ ), one can see that the matching of data obtained from the experiments and numerical simulations is very good for  $H < H_c$  and notably worse for  $H > H_c$ .

#### IV. DISCUSSION AND CONCLUSION

The main issue we faced in the comparison between the results obtained in our BN experiment and the possible results of the nonequilibrium athermal RFIM numerical simulations was the identification of the appropriate values of the RFIM parameters (lattice sizes, disorder  $R$ , and driving rate  $\Omega$ ) that would provide a reasonable matching of the two types of data.

To this end, we performed the simulations on the  $32\,768 \times 2048 \times 8$  striplike cubic lattice, the largest one we could use. This lattice with more than half a billion spins has approximately the same aspect ratio as the sample used in our experiment, which is important because the simulational results are affected by the lattice aspect ratio and also by the lattice finite size [55,56,58,62]. These two facts prevented us to use a bigger lattice (e.g., doubled along each of its sides) because seeking the reasonable  $(R, \Omega)$  pairs would be out of our reach due to the greatly increased running time of simulations at the corresponding computer memory demands.

Regarding the optimality of the value of disorder and the set of values of the driving rate in simulations for which the comparison with experimental findings is performed, we point out that these values depend on the choice of lattice (i.e., they might be somewhat different for another lattice due to the conformity of the finite-size and driving-rate scaling conditions [62]). It is also important to stress that the type and structure of the underlying sample affect the model's applicability. This is in particular because the employed version of the RFIM is not a realistic model for the Barkhausen noise recorded from the ferromagnetic samples having well-defined domain structure because, instead of considering the time evolution of magnetic domain pattern of driven disordered ferromagnetic samples responsible for the emission of BN, the model treats individual spins with the simplest mutual exchange coupling

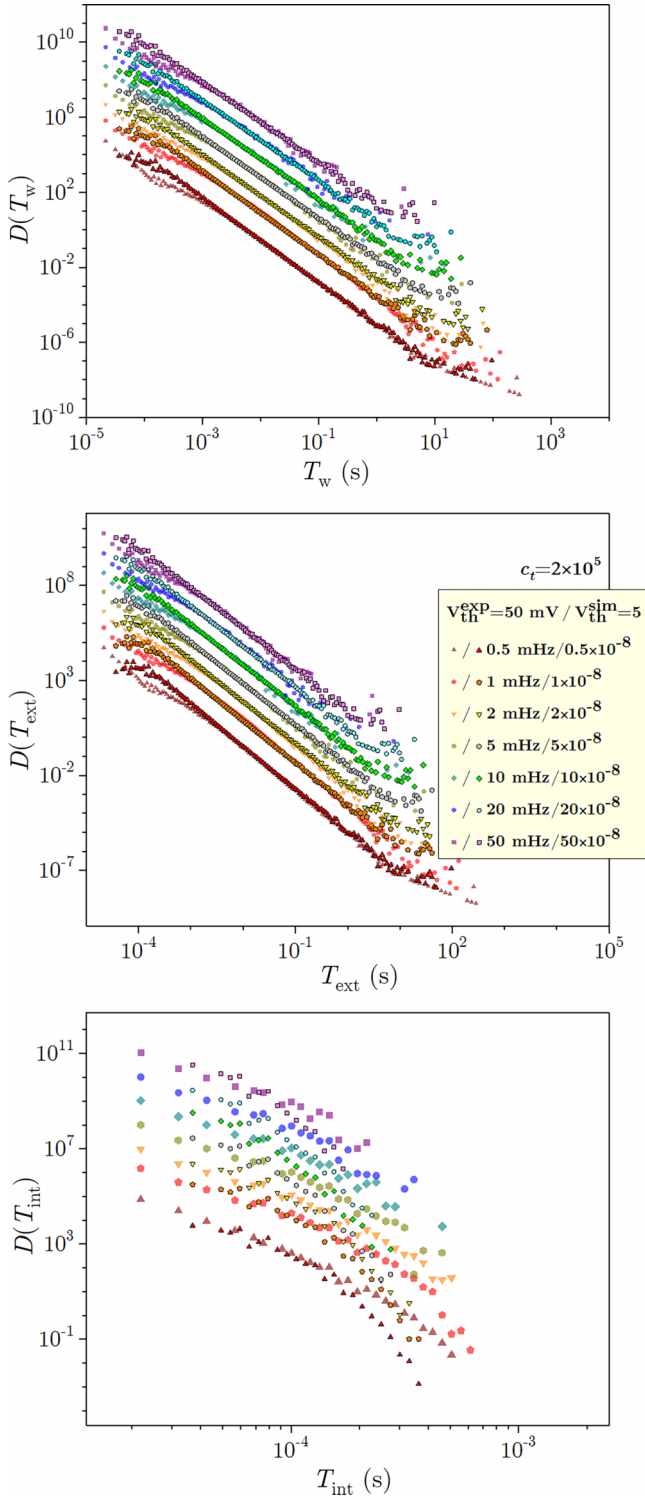


FIG. 11. Comparison of integrated distributions of total, external and internal waiting times, respectively, obtained in experiments and numerical simulations. The underlying data sets and all other parameters are the same as in Fig. 8.

and the coupling with the quenched random magnetic field whose existence and characterization in real samples is still not well documented and understood. Yet, as we demonstrated by a methodical comparison of the obtained simulational and

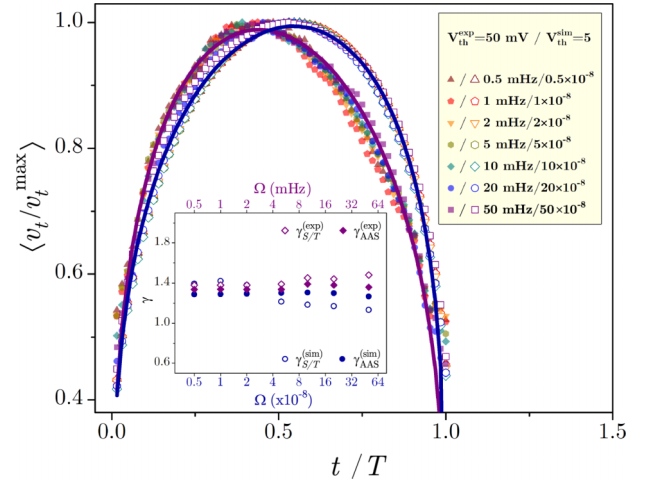


FIG. 12. Average avalanche shapes, shown by filled symbols, obtained from the experimental data and by empty symbols, obtained from the simulational data. The graph shows against  $t/T$  (i.e., time  $t$  measured from the start of avalanche scaled by avalanche duration  $T$ ) the values of  $\langle v_t / v_t^{\max} \rangle$  (i.e., the average value of the response signal  $v_t$  scaled by its maximum value  $v_t^{\max}$  during the avalanche). The underlying data sets and all other parameters are the same as in Fig. 8. Full lines are fits to the functional form (12) and the inset shows the comparison of  $\gamma_{S/T}$ , introduced in Eq. (5), to  $\gamma_{AAS}$  values, introduced in Eq. (12), for both simulations and experiment.

experimental results over a wide range of driving rates, in the case of nanocrystalline samples, this model shows a high degree of plausibility, reproducing most of the features obtained in the experimental measurements. Therefore, based on all our findings, we can consider that the athermal nonequilibrium RFIM version proved to be valuable for the comparison between its predictions and the characteristics of the Barkhausen noise emitted from the nanocrystalline samples.

To conclude, in this paper we systematically compared the findings of the Barkhausen noise measurements and the simulations of the nonequilibrium athermal RFIM. The measurements were performed on a VITROPERM 800 R metallic glass nanocrystalline strip driven by the external magnetic field at the rates between 0.5 and 50 mHz. All RFIM simulations were accomplished using suitable model parameters (lattice sizes with the aspect ratio as for the sample, a single value of disorder of the quenched random field, and a two-decade-wide range of driving). Applying these adjustments in simulations, allowed us to achieve a considerable matching with the experimental data. We hope that our findings will be helpful in the interpretation and analysis of experimental results obtained from a variety of striplike disordered ferromagnetic nanocrystalline samples driven at constant rates. Further on, the results of our study may also stimulate some future theoretical research, invoking the development of models that will more accurately capture the essence of the BN underlying dynamics.

#### ACKNOWLEDGMENTS

We acknowledge the support by the Ministry of Science, Technological Development and Innovation of Republic of



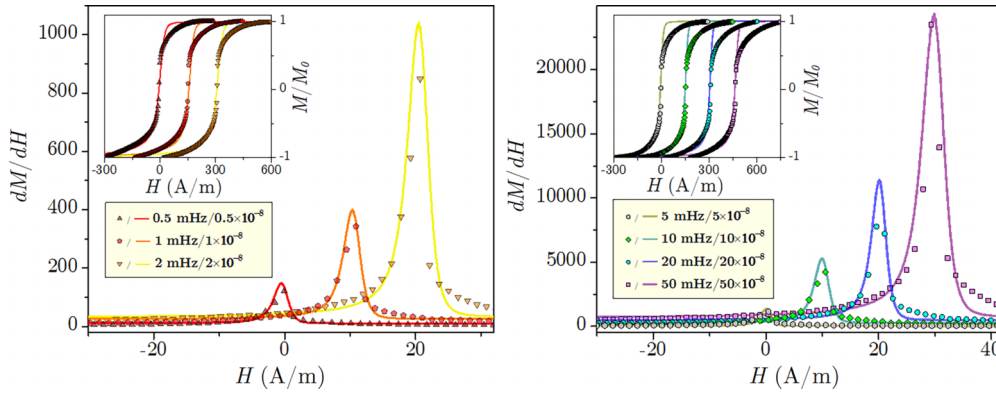


FIG. 13. Comparison of averaged magnetization and magnetic susceptibility curves obtained in experiments (symbols) and numerical simulations (full lines), the later scaled so as to achieve a matching with the experimental. The underlying data sets and other relevant parameters are the same as in Fig. 8. In the main panels, we show the magnetic susceptibilities  $dM/dH$  against the external magnetic field  $H$ , while in the insets we show  $M/M_0$  (i.e., the magnetization  $M$  scaled by the saturation magnetization  $M_0$ ) against  $H$ ; both types of curves correspond to the rising part of the hysteresis loop, and the  $dM/dH$  experimental curves are inverted (i.e., multiplied by  $-1$ ), cf. Fig. 2. In main panels and insets the curves are shifted for better visibility, namely susceptibilities and magnetizations in increments of  $10 \text{ Am}^{-1}$  and  $150 \text{ Am}^{-1}$  relative to the (unshifted) curves which correspond to the 0.5 and 5 mHz driving rates in left and right panel.

Serbia (Agreements No. 451-03-47/2023-01/200162 and No. 451-03-47/2023-01/200122). L.L. acknowledges the support of the Research Council of Finland via the Academy Project BarFume (Project No. 338955). A.D. acknowledges the support of the Serbian Academy of Sciences and Arts via the Grant No. F133. We thank the referees for their objections leading to modifications-clarifications of the original manuscript version posted on arXiv. We thank Dr. Tatjana Srećković from the Institute for Multidisciplinary Research, University of Belgrade, Republic of Serbia, for the thermal treatment of our samples, and Viktor Ćosić from Custom Electronics d.o.o., Belgrade, Republic of Serbia, for his assistance in overcoming certain instrument malfunctions.

#### APPENDIX A: COMPARISON OF BN RECORDINGS ACCOMPLISHED USING SHORT AND LONG PICKUP COILS

In inductive Barkhausen noise measurements, the response signal is collected with the aid of a pickup coil. One possibility is to use, like in the present experiment and Ref. [4], a long single-layered pickup coil tightly wound around the entire sample, or a multilayered short pickup coil, e.g., in Ref. [75], wound around the central part of the sample. As is illustrated in Fig. 14, the short pickup coil detects only the nearby changes in magnetization. This is not suitable for comparison with the cases in which the local changes in magnetization are homogeneously detected over the entire sample as in the RFIM model and the BN measurements performed with a long pickup coil.

Detection of the BN signal from the entire sample has been criticized in the literature (e.g., in Ref. [75]) on the grounds of a nonhomogeneous demagnetization field over the sample and informally also on the possibility that the current through the long pickup coil, triggered by some localized avalanche, may initiate by its flow another avalanche at some distant position that would otherwise be absent. This should not happen if the pickup coil is connected (like in our measurements) to the

amplifier with a large input impedance (say, above  $100 \text{ k}\Omega$ , so that the current induced in the pickup coil like ours remains below  $10 \text{ nA}$  and the corresponding magnetic field strength remains below  $0.1 \text{ mA/m}$ ). Regarding the first objection, according to our experience, the effect of the demagnetizing field  $H_{\text{dmf}} = -N_{\text{dmf}}M$  in the case of extended samples is low

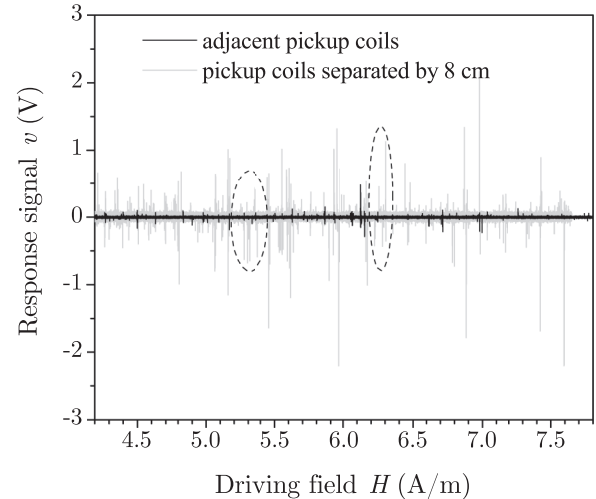


FIG. 14. Two sections of the BN response voltage signal  $v$  against driving magnetic field  $H$ . The sections were recorded at the 2-mHz driving frequency using two identical short pickup coils, whose length is 1 mm, with 300 turns connected in series but with opposite polarity (so that in both cases the overall signal is the sum of the EMFs induced in opposite directions). The black line shows the section from the signal recorded by the pickup coils placed next to each other so that the induced EMFs practically cancel each other. The gray line shows the section from the signal recorded by the pickup coils separated by 8 cm. Two encircled segments in this section show time-separated parts of opposite polarity caused by the changes in the magnetization localized near the first and the second pickup coil, respectively.

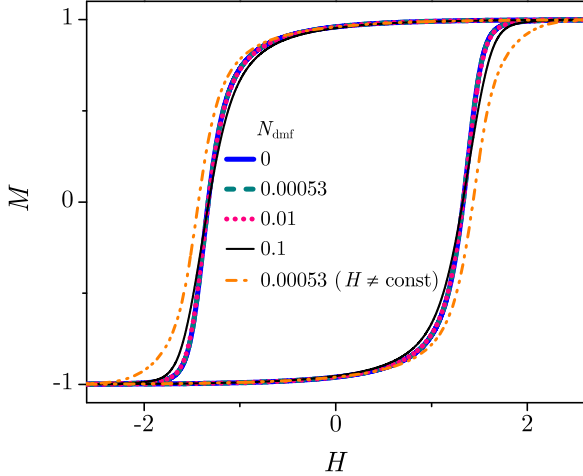


FIG. 15. Hysteresis loops for several values of the demagnetizing factor  $N_{\text{dmf}}$  from the legend. The loops are obtained in the athermal RFIM simulations on the  $16384 \times 1024 \times 4$  lattice (with approximately the same aspect ratios as for our sample) at the driving rate  $\Omega = 0.001$  and disorder  $R = 2.4$  of the quenched random field  $h_i$ . For the four first-listed loops the external magnetic field  $H = \text{const}$  over the entire sample (as is in the measurements we performed due to the use of compensating coils placed at the ends of the driving solenoid). Without compensating coils, at the ends of the sample (like the one used in Ref. [75]),  $H$  drops to 65% from its value at the middle, and such variation of  $H$  over the sample gives rise to noticeable changes in the hysteresis loop. On the other hand, if  $H = \text{const}$ , then the changes in the hysteresis loop become noticeable only for the values of  $N_{\text{dmf}}$  that are (about) 100 times greater than the value for our sample  $N_{\text{dmf}} = 0.00053$ .

due to the small demagnetizing factor  $N_{\text{dmf}}$  ( $=0.00053$  in our case) which we illustrate in Fig. 15. Here, however, we mention that if the external driving field  $H$  is not homogeneous over the entire sample, then a more pronounced effect could appear, as is shown in Fig. 15 by a dash-dotted (orange) line.

An additional difference between the long and short pickup coil appears in their amplitude-frequency response illustrated in Fig. 16. Comparing the impedance  $|Z|$  of the long coil (used in our experiment) with that of a short coil with 300 turns and the same resistance, one can see that the impedance of the long coil is flat in a broader range of frequencies potentially enabling usage of a low-pass filter with higher cutoff frequency, i.e., the measurements in an extended frequency range.

Despite the previous differences, recordings performed by using both types of pickup coils lead to essentially the same findings regarding the exponents characterizing the distributions of BN avalanches. This we illustrate in the main panels of Fig. 17 showing an overlapping between the corresponding distributions of avalanche size and duration collected with the aid of long and short pickup coils. Fits to the stretched exponential functional form

$$D_{SE}(X) = AX^{-a} \exp[-(X/X_0)^b], \quad (\text{A1})$$

where  $X$  is the avalanche parameter,  $A$  the function amplitude,  $a$  the pertinent exponent,  $X_0$  the cutoff parameter and  $b$  the cutoff exponent, are commonly used to estimate the pertinent exponents. In the insets of top-left and

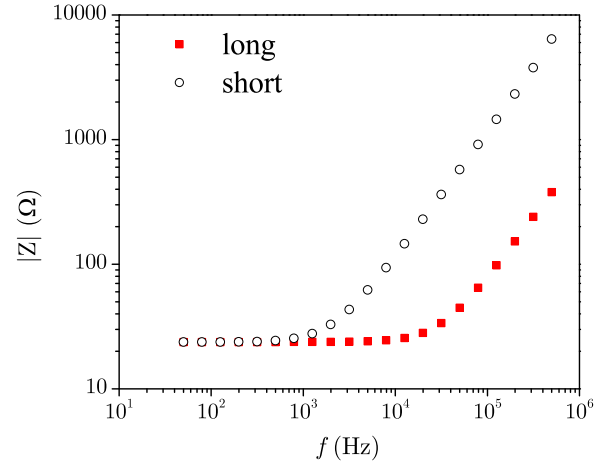


FIG. 16. Impedance  $|Z|$  (measured up to 500 kHz by a Microtest 6366 LCR meter) against frequency  $f$  for long pickup coil used in our experiment (full symbols) and a short pickup coil (empty symbols) with the same resistance and 300 turns. As a matter of principle, an unbiased detection of the recorded signal is enabled in the range of frequencies in which the overall response of the pickup coil and amplifier is reasonably constant, whereas the frequency components in the detected signals outside this range should be suppressed by filtering. Our measurement data indicate that the resonance and antiresonance frequencies for both coils lie above 500 kHz. So the signal detection by both coils is safe below 100 kHz due to flat overall response provided in a frequency range wider than shown here by the used amplifier having (reasonably) high input impedance.

bottom-left panels of Fig. 17 are shown fits of both integrated and binned distributions (the distributions collected in a bin, i.e., a narrow window of the external magnetic field, where the response signal can be considered stationary), giving the exponent values  $\tau \sim 1.65/\tau_{\text{int}} \sim 1.93$  for the size distribution, and  $\alpha \sim 1.85/\alpha_{\text{int}} \sim 2.4$  for the duration distribution, binned, and integrated, respectively. Obtained values show that the BN, emitted from the VITROPERM 800 R sample, likely belongs to the same universality class as for the unstressed samples referenced in Ref. [75] and furthermore support the quasi-2D behavior of avalanches spreading in a sandwiched geometry within thin systems, which has been numerically explored earlier [55–58]. The impact of the bin width on the binned distribution is displayed in the insets of the top-right and bottom-right panels of Fig. 17. It is evident that for the narrow bins, containing a small percentage of the magnetization saturation value (10% or less), the distributions are independent of the bin width, while as the bin size increases, the distributions tend towards the integrated one. Additionally, a closer inspection of Fig. 17 reveals that the long pickup coil seems to be more efficient in detection of small (but not the smallest) avalanches giving steeper distributions in their initial part weakly affected by the choice of threshold, as is predicted for thin samples in RFIM simulations [55–58].

## APPENDIX B: ON THE ADEQUACY OF USING THE RFIM FOR BN SIMULATIONS

Barkhausen noise emissions are theoretically usually described as a consequence of a jerky motion of the magnetic

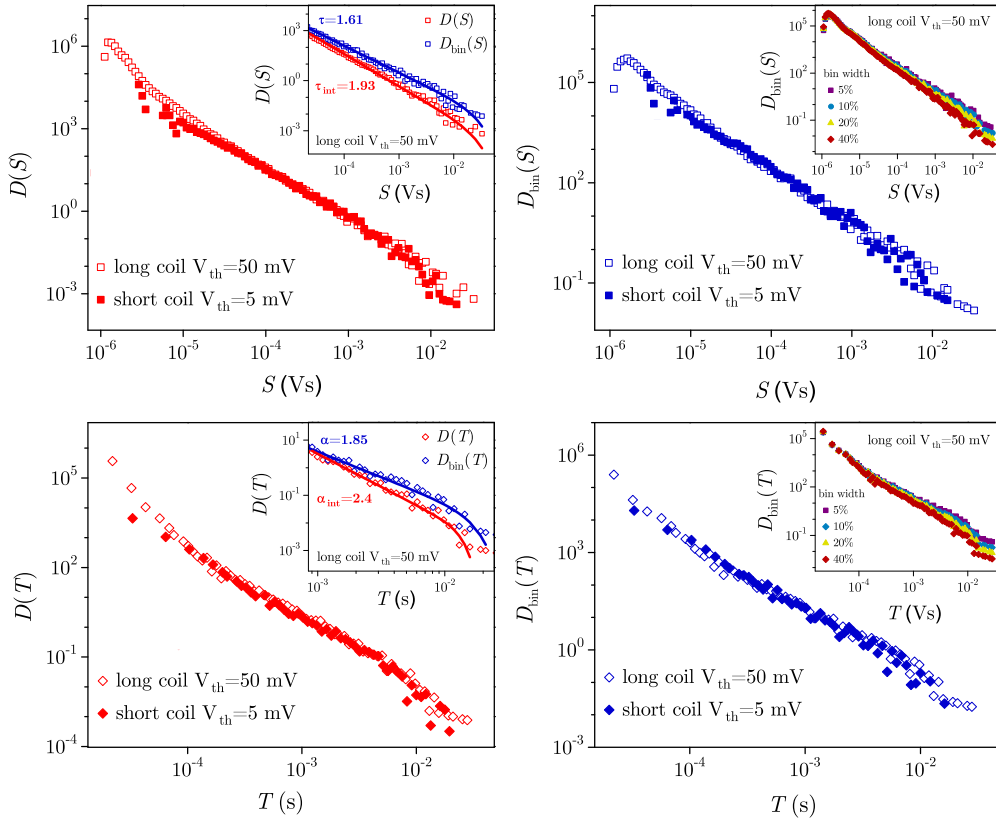


FIG. 17. Main panels present a comparison of integrated size distributions (top-left), binned size distributions (top-right), integrated duration distributions (bottom-left), and binned duration distributions (bottom-right) collected by the long pickup coil (empty red squares) and by the short pickup coil (full black circles). Binned distributions are collected in the window that is centered at the coercive field  $H_{\text{coerc}}$  (i.e., the value of  $H$  at which magnetization  $M = 0$ ) and has width such that magnetization changes within it by 10% of saturation value. Insets of top-left and bottom-left panels show fits to the functional form (A1) of both integrated and binned distributions obtained from the recordings using the long pickup coil, giving the exponent values  $\tau \sim 1.65/\tau_{\text{int}} \sim 1.93$  for the size distribution, and  $\alpha \sim 1.85/\alpha_{\text{int}} \sim 2.4$  for the duration distribution, respectively. Insets of top-right and bottom-right panels demonstrate the variation of the binned distribution with the selected bin width expressing the change of magnetization in bin as a percentage of the magnetization saturation value. Recording settings: 16 cm  $\times$  1 cm  $\times$  40  $\mu\text{m}$  VITROPERM 800 R sample, triangular profile of the external magnetic driving field with 550 A/m amplitude and 2 mHz driving rate; the BN signal, amplified 2000 times and low-pass filtered at 100 kHz, is sampled at 200 kSa/s sampling rate with 16-bits resolution. Due to approximately 10 times smaller sensitivity of the short pickup coil, the corresponding distributions are extracted at 10 times  $V_{\text{th}}$  and appropriately shifted to achieve overlapping with the distributions collected with the long pickup coil.

domain walls in the ferromagnetic samples with impurities or imperfections. In this respect, one may ask a question whether the RFIM is a suitable candidate for the description of the BN emissions. Indeed, the RFIM treats the discrete system of spins having only two possible orientations (+1 and -1) so that instead of continuously spreading magnetic domains there are only clusters of discrete spins of the same orientation and there are no domain walls (i.e., thin regions separating two neighboring domains in which the local magnetization gradually changes between the orientations of the neighboring domains). For this reason, the RFIM is not suitable for the description of the BN in materials with a well-developed domain structure.

However, the situation becomes different for materials with nanocrystalline grains. Experimental studies [76–78] have shown that the grains in such materials behave like single-domain particles and that the boundaries of crystal grains may play the role of quenched and random pinning centers which are likely to be normally distributed due to many small factors present during the melt-spinning technique of the

sample production. Although due to this production method the grains are not regularly distributed in space (see, e.g., Product details tab in Ref. [79]), for simplicity here we treat them to be positioned on the (nonequilateral) 3D cubic lattice.

As the Curie temperature for VITROPERM 800 R is  $T_c = 600^\circ\text{C}$ , the magnetization of its grains at room temperatures is close to the saturation value and is dominantly parallel to the longitudinal axis of the sample which is its easy axis of magnetization. Magnetic interaction of the grains is of the dipole-dipole type but, owing to the relatively large separation between the dipole centers, may be coarsely considered to affect only nearby dipoles. For these reasons, and due to a narrow Gaussian distribution of grain size (ranging between 10 and 15 nm), the RFIM may be considered to be a suitable model, specifically its athermal nonequilibrium version for the reasons already mentioned in the penultimate paragraph of Sec. I and the first paragraph of Sec. III C 2, respectively. In this respect, the question about the most appropriate choice of the random field is of minor importance because the model behavior is essentially not affected by this choice [44,45] and,

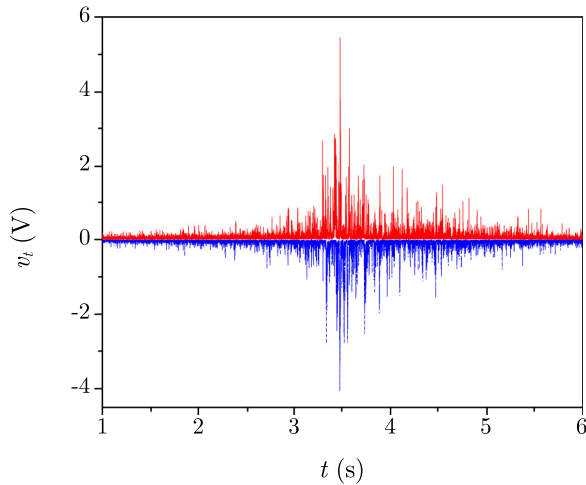


FIG. 18. Time sequences of the BN signal  $v_t$  extracted at the same position on the rising part of two adjacent cycles of the external field  $H$ ; the signal shown by the full (red) line is here inverted for the sake of easier comparison with the one from the next cycle shown by the dashed (blue) line. Although the sequences are rather similar, their differences are noticeable.

therefore in this work, we used the normal distribution as the most standard.

Nevertheless, one can also pose an additional objection which reads: RFIM is a fully deterministic model, meaning that once the random quenched field  $h_i$  is chosen the system will exactly repeat its response when cycled by the external magnetic field. This is not the case for the real BN emissions

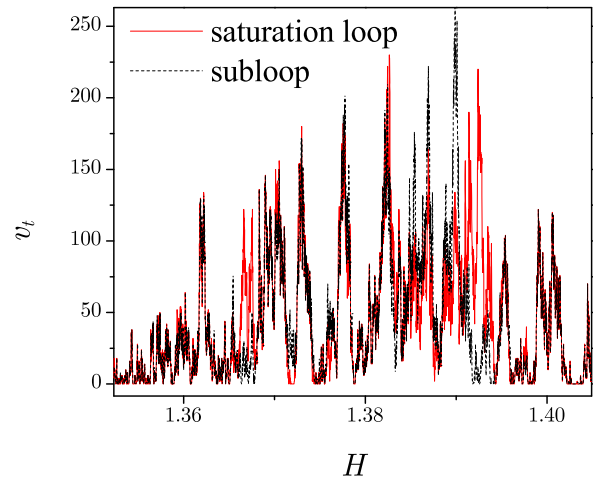


FIG. 19. The same as in Fig. 18, but for the RFIM response signal from the saturation loop (full red line) and its slightly smaller subloop in the next cycle (dashed black line).

as illustrated in Fig. 18 by two sections of the BN emissions recorded in the same window of the external magnetic field on the rising part of two adjacent cycles. Although their overall appearance is quite similar, on closer inspection the differences are noticeable. One of many possible causes might be a slightly different maximum of the driving field profile which should correspond to two different loops at the same random field configuration (e.g., saturation loop and its slightly smaller subloop) in simulations leading to somewhat different response signals, as is shown in Fig. 19.

- 
- [1] J. P. Sethna, K. A. Dahmen, and C. R. Myers, *Nature (London)* **410**, 242 (2001).
- [2] H. Barkhausen, Zwei mit Hilfe der neuen Verstärker entdeckte Erscheinungen, *Physische, Phys. Z.* **20**, 401 (1919).
- [3] B. Alessandro, C. Beatrice, G. Bertotti, and A. Montorsi, Domain-wall dynamics and Barkhausen effect in metallic ferromagnetic materials. II. Experiments, *J. Appl. Phys.* **68**, 2908 (1990).
- [4] D. Spasojević, S. Bukvić, S. Milošević, and H. E. Stanley, Barkhausen noise: Elementary signals, power laws, and scaling relations, *Phys. Rev. E* **54**, 2531 (1996).
- [5] M. Bahiana, B. Koiller, S. L. A. de Queiroz, J. C. Denardin, and R. L. Sommer, Domain size effects in Barkhausen noise, *Phys. Rev. E* **59**, 3884 (1999).
- [6] A. P. Mehta, A. C. Mills, K. A. Dahmen, and J. P. Sethna, Universal pulse shape scaling function and exponents: Critical test for avalanche models applied to Barkhausen noise, *Phys. Rev. E* **65**, 046139 (2002).
- [7] F. Colaioni, S. Zapperi, and G. Durin, Shape of a Barkhausen pulse, *J. Magn. Magn. Mater.* **272-276**, E533 (2004).
- [8] G. Durin and S. Zapperi, Scaling exponents for Barkhausen avalanches in polycrystalline and amorphous ferromagnets, *Phys. Rev. Lett.* **84**, 4705 (2000).
- [9] E. Puppini, Statistical properties of Barkhausen noise in thin Fe films, *Phys. Rev. Lett.* **84**, 5415 (2000).
- [10] T. A. Moore, J. Rothman, Y. B. Xu, and J. A. C. Bland, Thickness-dependent dynamic hysteresis scaling behavior in epitaxial Fe/GaAs(001) and Fe/InAs(001) ultrathin films, *J. Appl. Phys.* **89**, 7018 (2001).
- [11] E. Puppini, E. Pinotti, and M. Brenna, Barkhausen noise in variable thickness amorphous finemet films, *J. Appl. Phys.* **101**, 063903 (2007).
- [12] D.-H. Kim, S.-B. Choe, and S.-C. Shin, Direct observation of Barkhausen avalanche in Co thin films, *Phys. Rev. Lett.* **90**, 087203 (2003).
- [13] K.-S. Ryu, H. Akinaga, and S.-C. Shin, Tunable scaling behaviour observed in Barkhausen criticality of a ferromagnetic film, *Nat. Phys.* **3**, 547 (2007).
- [14] S.-C. Shin, K.-S. Ryu, D.-H. Kim, S.-B. Choe, and H. Akinaga, Power-law scaling behavior in Barkhausen avalanches of ferromagnetic thin films, *J. Magn. Magn. Mater.* **310**, 2599 (2007).
- [15] H.-S. Lee, K.-S. Ryu, K.-R. Jeon, S. S. P. Parkin, and S.-C. Shin, Breakdown of Barkhausen critical-scaling behavior with increasing domain-wall pinning in ferromagnetic films, *Phys. Rev. B* **83**, 060410(R) (2011).
- [16] F. Bohn, M. A. Corrêa, A. da Cas Viegas, S. Papanikolaou, G. Durin, and R. L. Sommer, Universal properties of magnetization dynamics in polycrystalline ferromagnetic films, *Phys. Rev. E* **88**, 032811 (2013).



- [17] F. Bohn, M. A. Corrêa, M. Carara, S. Papanikolaou, G. Durin, and R. L. Sommer, Statistical properties of Barkhausen noise in amorphous ferromagnetic films, *Phys. Rev. E* **90**, 032821 (2014).
- [18] G. Durin, F. Bohn, M. A. Corrêa, R. L. Sommer, P. Le Doussal, and K. J. Wiese, Quantitative scaling of magnetic avalanches, *Phys. Rev. Lett.* **117**, 087201 (2016).
- [19] F. Bohn, G. Durin, M. A. Corrêa, N. R. Machado, R. D. D. Pace, C. Chesman, and R. L. Sommer, Playing with universality classes of Barkhausen avalanches, *Sci. Rep.* **8**, 11294 (2018).
- [20] M. Honkanen, S. Santa-aho, L. Laurson, N. Eslahi, A. Foi, M. Vippola, Mimicking Barkhausen noise measurement by *in-situ* transmission electron microscopy—Effect of microstructural steel features on Barkhausen noise, *Acta Mater.* **221**, 117378 (2021).
- [21] J. Uhl, S. Pathak, D. Schorlemmer, X. Liu, R. Swindeman, B. A. W. Brinkman, M. LeBlanc, G. Tsekenis, N. Friedman, R. Behringer *et al.*, Universal quake statistics: From compressed nanocrystals to earthquakes, *Sci. Rep.* **5**, 16493 (2015).
- [22] S. Santucci, R. Planet, K. J. Måløy, and J. Ortín, Avalanches of imbibition fronts: Towards critical pinning, *Europhys. Lett.* **94**, 46005 (2011).
- [23] D. M. Dimiduk, C. Woodward, R. LeSar, and M. D. Uchic, Scale-free intermittent flow in crystal plasticity, *Science* **312**, 1188 (2006).
- [24] P. D. Ispanovity, L. Laurson, M. Zaiser, I. Groma, S. Zapperi, and M. J. Alava, Avalanches in 2D dislocation systems: Plastic yielding is not depinning, *Phys. Rev. Lett.* **112**, 235501 (2014).
- [25] S. Janičević, M. Ovaska, M. J. Alava, and L. Laurson, Avalanches in 2D dislocation systems without applied stresses, *J. Stat. Mech.* (2015) P07016.
- [26] P. D. Ispanovity, D. Ugi, G. Péterffy, M. Knapek, S. Kalácska, D. Tüzes, Z. Dankházi, K. Máthis, F. Chmelík, and I. Groma, Dislocation avalanches are like earthquakes on the micron scale, *Nat. Commun.* **13**, 1975 (2022).
- [27] P. Ch. Ivanov, L. A. N. Amaral, A. L. Goldberger, S. Havlin, M. G. Rosenblum, H. E. Stanley, and Z. R. Struzik, From 1/*f* noise to multifractal cascades in heartbeat dynamics, *Chaos: Interdiscip. J. Nonlin. Sci.* **11**, 641 (2001).
- [28] C.-C. Lo, L. A. N. Amaral, S. Havlin, P. Ch. Ivanov, T. Penzel, J.-H. Peter, and H. E. Stanley, Dynamics of sleep-wake transitions during sleep, *Europhys. Lett.* **57**, 625 (2002).
- [29] N. Friedman, S. Ito, B. A. W. Brinkman, M. Shimono, R. E. L. DeVille, K. A. Dahmen, J. M. Beggs, and T. C. Butler, Universal critical dynamics in high resolution neuronal avalanche data, *Phys. Rev. Lett.* **108**, 208102 (2012).
- [30] S. R. Miller, S. Yu, and D. Plenz, The scale-invariant, temporal profile of neuronal avalanches in relation to cortical  $\gamma$ -oscillations, *Sci. Rep.* **9**, 16403 (2019); see also *Criticality in Neural Systems*, edited by D. Plenz and E. Niebur (Wiley Online Library, 2014).
- [31] D. S. Fisher, Collective transport in random media: From superconductors to earthquakes, *Phys. Rep.* **301**, 113 (1998).
- [32] J. Davidsen and M. Baiesi, Self-similar aftershock rates, *Phys. Rev. E* **94**, 022314 (2016).
- [33] A. Bizzarri, A. Petri, and A. Baldassarri, Earthquake dynamics constrained from laboratory experiments: New insights from granular materials, *Ann. Geophys.* **64**, SE441 (2021).
- [34] J. Perelló, J. Masoliver, A. Kasprzak, and R. Kutner, Model for interevent times with long tails and multifractality in human communications: An application to financial trading, *Phys. Rev. E* **78**, 036108 (2008).
- [35] J. P. Bouchaud, Crises and collective socio-economic phenomena: Simple models and challenges, *J. Stat. Phys.* **151**, 567 (2013).
- [36] D. P. Belanger and T. Nattermann, *Spin Glasses and Random Fields*, edited by A. P. Young (World Scientific, Singapore, 1998), pp. 251–298.
- [37] J. P. Sethna, K. A. Dahmen, S. Kartha, J. A. Krumhansl, B. W. Roberts, and J. D. Shore, Hysteresis and hierarchies: Dynamics of disorder-driven first-order phase transformations, *Phys. Rev. Lett.* **70**, 3347 (1993).
- [38] O. Perković, K. A. Dahmen, and J. P. Sethna, Disorder-induced critical phenomena in hysteresis: Numerical scaling in three and higher dimensions, *Phys. Rev. B* **59**, 6106 (1999).
- [39] J. P. Sethna, K. A. Dahmen, and O. Perković, Random-field Ising models of hysteresis, in *The Science of Hysteresis*, edited by G. Bertotti and I. Mayergoyz (Academic Press, Amsterdam, 2006), pp. 107–179.
- [40] T. Herranen and L. Laurson, Barkhausen noise from precessional domain wall motion, *Phys. Rev. Lett.* **122**, 117205 (2019).
- [41] S. Kaappa and L. Laurson, Barkhausen noise from formation of 360° domain walls in disordered permalloy thin films, *Phys. Rev. Res.* **5**, L022006 (2023).
- [42] S. Zapperi, P. Cizeau, G. Durin, and H. E. Stanley, Dynamics of a ferromagnetic domain wall: Avalanches, depinning transition, and the Barkhausen effect, *Phys. Rev. B* **58**, 6353 (1998).
- [43] C. Frontera and E. Vives, Studying avalanches in the ground state of the two-dimensional random-field Ising model driven by an external field, *Phys. Rev. E* **62**, 7470 (2000).
- [44] Y. Liu and K. A. Dahmen, Unexpected universality in static and dynamic avalanches, *Phys. Rev. E* **79**, 061124 (2009).
- [45] Y. Liu and K. A. Dahmen, Random-field Ising model in and out of equilibrium, *Europhys. Lett.* **86**, 56003 (2009).
- [46] I. Balog, G. Tarjus, and M. Tissier, Criticality of the random field Ising model in and out of equilibrium: A nonperturbative functional renormalization group description, *Phys. Rev. B* **97**, 094204 (2018).
- [47] VITROPERM 800 materials are commercially used for common mode chokes for EMI filters in renewable energy, electric drives and motors, EV-charging and automotive, gate drive transformers and current transformers in electric drives and motors, and as shielding material in wireless power transfer.
- [48] S. Bukvić and Dj. Spasojević, An alternative approach to spectrum baseline estimation, *Spectrochim. Acta, Part B* **60**, 1308 (2005).
- [49] S. Bukvić, Dj. Spasojević, and V. Žigman, Advanced fit technique for astrophysical spectra, *Astron. Astrophys.* **477**, 967 (2008).
- [50] L. Laurson, X. Illa, and M. J. Alava, The effect of thresholding on temporal avalanche statistics, *J. Stat. Mech.* (2009) P01019.
- [51] G. Durin and S. Zapperi, *The Science of Hysteresis*, edited by G. Bertotti, and I. Mayergoyz (Academic Press, Amsterdam, 2006), pp. 181–267.
- [52] It is known that the exponent value extracted through the linear fit applied in the scaling region can be significantly influenced

- by the presence of the cutoffs. More reliable exponent values are obtained by fitting the data to a suitably chosen model function reasonably describing the cutoffs, see, e.g., in Ref. [73] the analytic form (15) describing the cutoff function.
- [53] D. Spasojević, S. Janičević, and M. Knežević, Avalanche distributions in the two-dimensional nonequilibrium zero-temperature random field Ising model, *Phys. Rev. E* **84**, 051119 (2011).
- [54] D. Spasojević, S. Janičević, and M. Knežević, Numerical evidence for critical behavior of the two-dimensional nonequilibrium zero-temperature random field Ising model, *Phys. Rev. Lett.* **106**, 175701 (2011).
- [55] D. Spasojević, S. Mijatović, V. Navas-Portela, and E. Vives, Crossover from three-dimensional to two-dimensional systems in the nonequilibrium zero-temperature random-field Ising model, *Phys. Rev. E* **97**, 012109 (2018).
- [56] S. Mijatović, D. Jovković, S. Janičević, and D. Spasojević, Critical disorder and critical magnetic field of the nonequilibrium athermal random-field Ising model in thin systems, *Phys. Rev. E* **100**, 032113 (2019).
- [57] B. Tadić, S. Mijatović, S. Janičević, Dj. Spasojević, and G. J. Rodgers, The critical Barkhausen avalanches in thin random-field ferromagnets with an open boundary, *Sci. Rep.* **9**, 6340 (2019).
- [58] S. Mijatović, M. Branković, S. Graovac, and D. Spasojević, Avalanche properties in striplike ferromagnetic systems, *Phys. Rev. E* **102**, 022124 (2020).
- [59] S. Janičević, D. Knežević, S. Mijatović, and D. Spasojević, Scaling domains in the nonequilibrium athermal random field Ising model of finite systems, *J. Stat. Mech.* (2021) 013202.
- [60] B. Tadić, Dynamic criticality in driven disordered systems: Role of depinning and driving rate in Barkhausen noise, *Physica A* **270**, 125 (1999).
- [61] R. A. White and K. A. Dahmen, Driving rate effects on crackling noise, *Phys. Rev. Lett.* **91**, 085702 (2003).
- [62] S. Radić, S. Janičević, D. Jovković, and D. Spasojević, The effect of finite driving rate on avalanche distributions, *J. Stat. Mech.* (2021) 093301.
- [63] D. Spasojević and S. Janičević, Two-dimensional ferromagnetic systems with finite driving, *Chaos Solit. Fractals*. **158**, 112033 (2022).
- [64] D. Spasojević, S. Radić, D. Jovković, and S. Janičević, Spin activity correlations in driven disordered systems, *J. Stat. Mech.* (2022) 063302.
- [65] M. Kuntz, O. Perković, K. A. Dahmen, B. W. Roberts, and J. P. Sethna, Hysteresis, avalanches, and noise, *Comput. Sci. Eng.* **1**, 73 (1999).
- [66] R. J. Glauber, Time-dependent statistics of the Ising model, *J. Math. Phys.* **4**, 294 (1963).
- [67] K. Kawasaki, Diffusion constants near the critical point for time-dependent Ising models, *Phys. Rev.* **145**, 224 (1966).
- [68] R. H. Swendsen and J. S. Wang, Nonuniversal critical dynamics in Monte Carlo simulations, *Phys. Rev. Lett.* **58**, 86 (1987).
- [69] F. J. Pérez-Reche and E. Vives, Finite-size scaling analysis of the avalanches in the three-dimensional Gaussian random-field Ising model with metastable dynamics, *Phys. Rev. B* **67**, 134421 (2003).
- [70] F. J. Pérez-Reche and E. Vives, Spanning avalanches in the three-dimensional Gaussian random-field Ising model with metastable dynamics: Field dependence and geometrical properties, *Phys. Rev. B* **70**, 214422 (2004).
- [71] D. Spasojević, S. Janičević, and M. Knežević, Analysis of spanning avalanches in the two-dimensional nonequilibrium zero-temperature random-field Ising model, *Phys. Rev. E* **89**, 012118 (2014).
- [72] M. C. Kuntz and J. P. Sethna, Noise in disordered systems: The power spectrum and dynamic exponents in avalanche models, *Phys. Rev. B* **62**, 11699 (2000).
- [73] A. Rosso, P. Le Doussal, and K. J. Wiese, Avalanche-size distribution at the depinning transition: A numerical test of the theory, *Phys. Rev. B* **80**, 144204 (2009).
- [74] L. Laurson, X. Illa, S. Santucci, K. T. Tallakstad, K. J. Måløy, and M. J. Alava, Evolution of the average avalanche shape with the universality class, *Nat. Commun.* **4**, 2927 (2013).
- [75] G. Durin and S. Zapperi, The role of stationarity in magnetic crackling noise, *J. Stat. Mech.* (2006) P01002.
- [76] L. Małkiński and A. Ślawska-Waniewska, Barkhausen jumps in FeCrCuNbSiB nanocrystalline alloy, *J. Magn. Magn. Mater.* **157-158**, 195 (1996).
- [77] L. Małkiński and A. Ślawska-Waniewska, Temperature dependence of the Barkhausen noise in Fe<sub>66</sub>Cr<sub>8</sub>Cu<sub>1</sub>Nb<sub>3</sub>Si<sub>13</sub>B<sub>9</sub> nanocrystalline alloy, *J. Magn. Magn. Mater.* **160**, 273 (1996).
- [78] Q. Li, C. W. Kartikowati, S. Horie, T. Ogi, T. Iwaki, and K. Okuyama, Correlation between particle size/domain structure and magnetic properties of highly crystalline Fe<sub>3</sub>O<sub>4</sub> nanoparticles, *Sci. Rep.* **7**, 9894 (2017).
- [79] <https://vacuumschmelze.com/products/soft-magnetic-materials-and-stamped-parts/nanocrystalline-material-vitroperm>